Elsevier Editorial System(tm) for Remote Sensing of Environment
Manuscript Draft

Manuscript Number:

Title: A revised L-band radio-brightness sensitivity to extreme winds under Tropical Cyclones: the 5 years SMOS-storm database

Article Type: SMOS 5 Years

Corresponding Author: Dr Nicolas REUL,

Corresponding Author's Institution:

First Author: Nicolas REUL

Order of Authors: Nicolas REUL; bertrand Chapron; yves quilfen; elizabetha Zabolotskikh; sebastien guimbard; jean-francois piolle; craig donlon

Highlights

- 5 years of SMOS radiometer L-band data intercepts with Tropical Cyclones are analysed
- . The storm-induced brightness contrast ΔI monotonically increases with their intensity
- In average, the brightest ΔI are found in the right-hand side quadrants of the storms
- A quadratic relationship relates ΔI and the 10 m height surface wind speed (SWS)
- SWS can be retrieved from SMOS with an rms error of 5 m/s up to 50 m/s

A revised L-band radio-brightness sensitivity to extreme winds under Tropical Cyclones: The 5 years SMOS-storm database

N.Reul [1], B. Chapron[1],Y.Quilfen[1], E.Zabolotskikh[2], S. Guimbard[1], J.F Piolle[1] and C.Donlon[3]

Authors affiliations:

(1) N.Reul, B. Chapron, Y. Quilfen, S. Guimbard and J.F. Piolle are with the Laboratoire d'Océanographie Spatiale, Institut Français de Recherche et d'Exploitation de la MER (IFREMER), Centre Bretagne - ZI de la Pointe du Diable - CS 10070 - 29280 Plouzané, France. nreul@ifremer.fr

(2) E.Zabolotskikh is with Satellite Oceanography Laboratory, Russian State Hydrometeorological University (RSHU), Malookhtinsky prosp., 98, St. Petersburg, Russia, 195196

(3) C. Donlon is with European Space Agency, ESTEC, Earth Observation Programmes, Mission Science Division, Keplerlaan 1, 2200 AG Noordwijk, The Netherlands

Manuscript submitted in Aug 2015 to RSE special journal issue on SMOS "ESA's Soil Moisture and Ocean Salinity Mission: Achievements and novel applications after 5 years in orbit"

Abstract

Five years of SMOS L-band brightness temperature data intercepting a large number of Tropical Cyclones (TC) are analysed. The storm-induced half-power radio-brightness contrasts ΔI (differences between the brightness observed at some wind force and the one of the smooth water surface with the same physical parameters) have been estimated for ~300 SMOS intercepts of TCs, and further expressed in a common storm-centric coordinate system. As found, the mean brightness contrasts monotonically increase with storm intensities from about 5K for tropical storms to ~22K for the most intense category 5 TCs, illustrating the strong potential of SMOS data to help better monitoring TC intensification. A remarkable feature of the 2D mean ΔI fields and their variability is that maxima are systematically found on the right quadrants of the storms, consistent with the reported asymmetric structure of the wind and wave fields in hurricanes. An empirical Geophysical Model Function is further derived using a large ensemble of co-located SMOS ΔI, aircraft and analysed H*Wind surface wind speed data, revealing a quadratic relationship between the ΔI and the 10 m height surface wind speed U10. Using co-located rain rate estimates, we also show that the L-band radio-brightness contrasts might be weakly affected by rain or ice-phase clouds. Neglecting that impact, we compared SMOS, ECMF and NCEP winds to a large ensemble of H*WIND 2D fields to confirm that the surface wind speed in TCs can effectively be retrieved from SMOS data with an rms error on the order of 4-5 m/s up to 50 m/s. The SMOS wind speed products above hurricane force (32 m/s) are generally much more accurate than the one from NWP and ASCAT products, which are found to largely and systematically underestimate the surface wind speed in these extreme conditions.

1 INTRODUCTION

The measurement of surface wind speed in Tropical Cyclone (TC) is of primary importance for improving storm tracks and intensity forecasts but getting accurate direct, and remote, measurements at sea surface level still remain very challenging in these extreme conditions (Powell, 2010). With active remote sensing methods of wind measurement saturating in hurricane force winds (e.g., Donelly et al., 1999) and heavily suffering from rain contamination in the TC's eyewall and outer rainband regions (Weissman et al., 2002), microwave radiometry has played an important role in recent years. The Stepped Frequency Microwave Radiometer (SFMR) thus became National Oceanic and Atmospheric Administration (NOAA)'s primary airborne sensor for estimating surface wind speed in hurricanes (Uhlhorn et al., 2007). SFMR instrument measures the brightness temperature of the ocean at a number of C-band frequencies, including frequencies that permit the measurement, and correction for, both rain and surface wind speed. However, SFMR is limited as it operates only in the North Atlantic and Eastern Pacific, and mostly sample storms at reachable distances from the coasts. However, there is still no equivalent sensor capability in space today and most available active and passive orbiting sensors operating in the low microwave frequency bands show poor surface wind speed retrieval performances above hurricane force, mostly because of the difficulty to precisely separate wind from rain effects (Powell, 2010). Promising new approaches are nevertheless currently under development based on either the new capabilities of the Advanced Microwave Scanning Radiometer 2 (AMSR2) onboard the GCOM-W satellite (Zabolotskikh et al., 2015), or the exploitation of the active cross-polarization C-band SAR data (see Horstmann et al., 2013), and, in the near future, with the launch of the CYGNSS mission with principle based on GPS bistatic scatterometry at L-band (Ruf et al., 2013). The method developed by Zabolotskikh et al., 2015 to retrieve sea surface wind speed and rain in tropical cyclones involves the combination of brightness temperature data acquired at the six C- and X-band channels of AMSR-2. Contrarily to the previous AMSR and AMSR-E sensor series, which only operated a single ~6.9 GHz channel, AMSR-2 is now also equipped with an additional C-band channel at 7.3 GHz (originally installed for radio-frequency interferences mitigation). Taking advantage of the information from this new channel, the multi-frequency algorithm developed has been shown to efficiently help to separate the wind and rain contributions in TC, the latest still strongly affecting each single C-band channel signals.

Because upwelling radiation at 1.4 GHz (L-band) is significantly less affected by rain and atmospheric effects than at higher microwave frequencies (Reul et al., 2012), L-band passive and active measurements from the European Space Agency Soil Moisture and Ocean Salinity (SMOS), the NASA Aquarius-SAC/D and the recently launched Soil Moisture Active Passive (SMAP) missions offer new unique opportunities to complement existing ocean satellite high wind observations in tropical cyclones and severe weather. SMOS provides multi-angular L-band brightness temperature images of the Earth over a ~1000 km swath at about ~43 km nominal resolution. SMAP performs simultaneous measurement of L-band brightness temperature and backscatter, at spatial resolutions of about 40 km across the entire swath (~1000km wide) and 3 km over outer 70% of the swath, respectively (Entekhabi et al., 2014). Thanks to their large swaths, both missions provide data with global coverage in about 3-days. Aquarius sensor capabilities were limited in the context of TC surface wind speed retrieval because of the low spatial resolution of the instruments (~100 km) and the relatively narrow width of their swaths (~300 km when combining all 3 beams), providing global revisit time of only 7 days. While the combination of passive and active L-band sensors is certainly very promising for surface wind speed remote sensing in extreme conditions, in this paper, we shall focus only on the brightness temperature signatures of tropical cyclones as observed by SMOS radiometer over 2010-2015.

A first demonstration that SMOS L-band passive data could be used to retrieve meaningful surface wind speed in tropical cyclones and storms has been provided in [Reul et al., 2012]. The L-band microwave brightness temperature contrast of the sea surface, defined as the difference between the brightness temperature observed at surface level at some wind force and the brightness temperature of the smooth water surface with the same physical parameters (temperature and salinity), were evaluated. The induced radio-brightness contrasts observed as the instrument intercepted IGOR storm at several stages of its evolution were co-located and compared to observed and modelled surface wind speed products. From this dataset, a first Geophysical Model Function (GMF) has been proposed to describe the relation of the half power L-band radio-brightness contrast $\Delta I = \Delta\,(Th+Tv)/2$ of the ocean with the surface wind speed modulus U. The radio-contrast ΔI was found to increase quasi-linearly with increasing wind speed with a significant change of sensitivity ($\partial\Delta I/\partial U$) from ~0.3 K/(m/s) below hurricane force (~32 m/s) to ~0.7 K/(m/s) above. That GMF was further used to retrieved surface wind speed from SMOS data over independent IGOR intercepts: the evolution of the retrieved maximum surface wind speed, the radii of 34, 50 and 64 knots surface wind speeds were shown to be consistent with hurricane model solutions and observation analyses. The authors concluded that neglecting potential rain and sea-state contributions to the signal, the surface wind speed modulus over ~50 km pixels can be retrieved in average with a root mean square error on the order of 5 m/s.

Impacts of heavy rain and ice clouds in the atmosphere on the L-band radio-brightness contrasts, as well as potential sea state effects remain however rather uncertain and could be sources of larger amplitude local errors on the retrieved surface wind speed.

The effects of rain and atmosphere in TC on radio emission from the sea surface is certainly weaker at L-band than it is at the higher frequencies (Reul et al., 2012). Atmospheric contributions dominated by absorption and emission due to oxygen at L-band can thus be corrected with negligible errors with respect the expected magnitude of the wind-induced surface radio-brightness contrasts. The absorption due to rain of upwelling radiations is also about a factor 100 more at C than it is at L band. Nevertheless, high wind region in TC are very often associated with extreme rain rates and atmosphere around the eyewalls is very often associated with high concentration of several hydrometeor species such as cloud water and ice, snow, and graupel (Houze et al., 1976). Small ice particles exist between the eyewall and outer rainbands, and graupel particles are collocated with the radius of maximum tangential wind (Houze et al., 1992). Hurricanes are usually glaciated everywhere above the −5°C level and the stratiform areas are dominated by snowflakes (aggregates) at these levels (Black and Hallett., 1986). The impacts of these ice phase cloud and of the concomitant high rain rate around the eyewall and rainbands in TCs on the L-band emission stay rather badly known. In Reul et al., 2012, an attempt to quantitatively evaluate the rain impact at a given wind speed was performed by classifying the estimated L-band radio-contrasts in rain-free and rainy conditions for four intercepts of IGOR, using co-localized rain rate measurements from various microwave sensors. Based on that limited amount of observations and previous radiative transfer simulations, we concluded that neglecting the contributions of rain to the L-band brightness temperature observed over the ocean at high winds shall be negligible in general, except in very high rain rates for which maximum rain impact can reach ∼4 K. Given the wind speed sensitivity of the SMOS GMF at high wind (~0.7 K/(m/s)), we concluded that neglecting rain effects could therefore induce wind speed retrieval errors up to ~6 m/s.

The brightness temperature of the ocean is strongly dependent on the foam coverage due to whitecap and streaks induced by wave breaking and wind tearing of the wave crest (Holthuijsen et al., 2012) but also on the distribution of foam formation thickness (Reul and Chapron, 2003). In addition, recent observations from Holthuijsen et al., 2012 suggest that the whitecap coverage is not increasing at hurricane wind force and above to reach a constant value of about 4%. The whitening observed above 33 m/s would thus be dominated by the growth of the streak coverage. Whether it is the increasing horizontal coverage of these streaks or the increasing thickness of the whitecaps, or a combination of both which explain the quasi-linear growth of the radio-brightness at L-band stays an open question. Both characteristics can be related to wind speed, but surface wave breaking and streak generation are also strongly dependent on sea surface wave growth, wave-wave and wave-current interaction, water depth and turning winds. The physics of the wave breaking generation process within hurricanes is complicated by the rapidly turning winds which generate cross-seas and higher sea state in the forward right-hand quadrant of the storms in the northern hemisphere (resp left-hand in the southern hemisphere). The velocity of forward movement of the storm, the maximum wind velocity and radius within the storm as well as the duration of wind action with respect group velocity of waves are key parameters known to play an important role in determining both the magnitude of the waves generated and also the spatial distribution of these waves within the storm quadrants (Young, 2003; MacAfee and Bowyer, 2005). The wave field is thus more asymmetric than the corresponding wind field, mainly due to the “extended fetch” which exists to the right of a translating hurricane due to relative wind/wave motions. It is worth noting that the effects of wave-current interaction on foam formations may also be of particular importance for hurricanes with landfall, e.g. in the US, due to the strong influence of either the Gulf Stream (Western Atlantic) or the Loop Current (Gulf of Mexico).

Yet, the impact of the variability of wave and wave breaking development in storm quadrants on the radio-brightness contrast at L-band are still very poorly known. Thus algorithms for wind speed retrieval from L-band microwave radiometry must be tested for sensitivity to these effects and corrected if necessary.

In this paper, we present results of a study conducted to extend the first demonstration presented in Reul et al., 2012 and to gain further insights into wind, rain and sea state effects. We systematically produced L-band SMOS radio-contrasts and high wind speed retrievals to generate a global database of SMOS intercepts with all world while TC events that developed over the period January 2010 to April 2015. Data and processing are described in a first section. In a second part, we show several examples of the SMOS signal and retrieved winds for various representative storms. In a third part, we analyse the statistical structural properties of the L-band brightness temperature contrasts as function of storm sectors and storm intensity. A subset of the SMOS-Storm database was selected for this purpose to include approximately 300 "best-quality" SMOS swath-storm intercepts with event intensities ranging from tropical storm to Category 5 in the Saffir-Simpson High Wind Scale (SSHWS). These intercepts data were selected following several criteria: 1) the storm center and its spatial domain within a radius of ~100-200 km had to be well observed by the instrument and 2) undetected/uncorrected Radio frequency interferences -and/or residual solar impacts on the brightness data were not affecting the retrieval quality significantly. Data were further classified following the storm intensity based on the value of the maximum sustained wind speed at the time of SMOS acquisitions, derived from Best-Track archive data. The position of the storm center and the bearing of the storm main motion at the time of SMOS acquisitions were determined and further used to map the storm brightness temperature contrast fields within a 1000×1000 km^2 box centered on each Storm eye location and rotated such that all storms are bearing towards a common direction. Average 2D properties of the L-band brightness temperatures per Saffir-Simpson categories are here analysed and presented, clearly illustrating the capability of L-band passive microwave data to provide a metric for intensity change in TCs.

In a fourth part, the SMOS retrieved winds based on the first GMF derived by Reul et al., 2012 are validated against SFMR flights and the NOAA/HWIND* analysed surface wind speed products. The quality of SMOS wind is assessed and compared to ECMWF and NCEP wind speed products in the range 0-50 m/s. Based on these co-localized data sets, a refined new GMF function is proposed.

In a last section we discuss the limitations and characteristics associated with such new observations (potential effects of rain and sea state and others) and the enhanced storm tracking capability that could come from merged SMOS-AMSR2 and SMAP data.

2 Data and Methods

2.1 SMOS data and processing

SMOS brightness temperature (T_B) images are formed through Fourier synthesis from the cross correlations between simultaneous signals obtained from pairs of antenna elements. For this study, we used the SMOS Level 1B V620 products, generated by the ESA/SMOS Data Processing Ground Segment (DPGS). The SMOS Level-1B product is the output of the image reconstruction of the observations and comprises the Fourier component of the brightness temperature in the antenna polarization reference frame, hence brightness temperatures. Level-1B corresponds to one temporal measurement, i.e., the whole field of view, one integration time, and is often called a 'snapshot' as for a camera. The brightness temperature images are further obtained by applying an inverse Fast Fourier Transform (IFFT) to the Level 1B brightness temperature Fourier coefficients using a Blackman spatial filter as described by Anterrieu et al. [2002]. The reconstructed brightness temperatures product at the top of the atmosphere is geolocated in an equal-area grid system (ISEA 4H9 - Icosahedral Snyder Equal Area projection) with an oversampled spatial resolution of about ~15 km. We consider here T_B data reconstructed in the extended field of view (FOV) domain of the antenna for which the swath width is approximately 1200 km [see Font et al., 2010, Figure 6]. The actual spatial resolution of the reconstructed T_B data varies within the FOV from ~32 km at boresight to about ~80 km at the edges of the swath (43 km on average over the field of view). The probing earth incidence angle is ranging from nadir to about 60° and the radiometric accuracy from 2.6 K at boresight to about 4–5 K on the swath edges. As the satellite moves, multiple observations of the same pixel at different incidence angles are obtained from successive snapshots. Earth grid points with less than 5 multiangular observations, as can be encountered at the extreme border of the swath, were removed.

The L-band brightness temperatures measured by a downward looking radiometer such as that on board SMOS are significantly influenced by a number of radiation sources [Yueh et al., 2001; Font et al., *2010*]. Among the most important sources of L-band brightness over the ocean are: (1) perfectly flat surface emission (with order of magnitude 100 K±4 K due to SSS & SST variability impact); (2) atmospheric emission (on the order of 5 K including reflected downwelling and upwelling); (3) scattered galactic radiation incident at the surface (order of magnitude 10 K); and (4) excess emission associated with the wind-driven surface roughness and breaking-wave generated foam (order of magnitude 10 K, up to 30 K in gale force winds).

By using the SMOS Level 2 radiative transfer forward model of scene brightness for each of these geophysical sources [Zine et al., 2008], we can estimate all but one of these contributions from the data in order to reveal individual residual sources ΔT_B of brightness contrast. To analyze SMOS signal over TCs and to reveal the impact of surface roughness and foam changes on the brightness temperatures at the radiometer, we therefore removed from the measurements all but the rough and foamy surface emission contributions. The necessary geophysical auxiliary data required to evaluate the different forward model contributions are obtained operationally at the SMOS measurement time and locations by the DPGS using products from ECMWF. Note that in the SMOS forward model [Zine et al., 2008], the evaluation of atmospheric contributions do not account for potential rain impact, which is hereafter neglected.

To estimate the flat sea surface emission contribution, we used the ECMWF/OSTIA Sea Surface Temperature daily nighttime products [Stark et al., 2007] and we estimated the sea surface salinity (SSS) using SMOS SSS data themselves for the week preceding the passage of the storms. For this study, we used the Centre Aval de Traitement des Données SMOS (CATDS, www.catds.fr) Expertise Center-Ocean Salinity SMOS SSS (IFREMER V02) Level 3 products [Reul and Ifremer CATDS-CECOS Team, 2011]. Data were first processed to provide a level 3 daily gridded SSS field at a resolution of 0.25° × 0.25° for the complete year. Composite weekly products were then generated for each storm using a running mean 7 days, 0.5° window. The SSS was further bi-linearly interpolated at 15 km resolution to evaluate the brightness contrast ΔT_B.

In Reul et al., 2012, we estimated that SSS errors on the order of ~0.5 psu, the accuracy of weekly CATDS products in the tropics, shall translate into maximum wind speed biases on the order of 1 m/s.

An additional source of earth surface emitted brightness modification at L-band as measured from space is the polarization mixing (Faraday rotation), due to the electromagnetic wave propagation through the ionosphere in the presence of the geomagnetic field [Skou, 2003]. It can be either modeled from the knowledge of the ionospheric Total Electron Content (TEC) and magnetic field or avoided by using the first Stokes parameter $I = T_H + T_V$, which is basically invariant by rotation. We chose here this alternative option and estimated the first Stokes surface roughness and foam-induced brightness temperature residual: $\Delta I = \Delta T_H + \Delta T_V$.

Finally, to reduce the instrument instantaneous radiometric noise which can vary from 2.6 K to 5 K for a single snapshot measurement as function of the position of the pixel within the swath, we averaged the SMOS multiangular measurements performed at a given location on earth to estimate an 'incidence-angle averaged' first Stokes brightness temperature residual generated by surface roughness and foam: : $\overline{\Delta I} = \frac{1}{\theta_{max}-\theta_{min}} \int_{\theta_{min}}^{\theta_{max}} \Delta I(\theta) d\theta$, where θ is the earth incidence angle and $[\theta_{min}, \theta_{max}] \approx [10°, 60°]$. Note that in the remaining of the paper, we will consider the half total power: $\frac{\Delta \bar{I}}{2} = \Delta(T_H + T_V)/2$ and for clarity, we shall drop the overbar notation. Unless specified, ΔI will therefore always refer to the incidence angle-averaged half-power quantity. The noise-reduction approach through incidence-angle averaging is necessary in the context of SMOS data analysis for instantaneous events because of the low signal-to-noise ratio for a single angle measurement. The approach is justified by the fact that a small incidence-angle dependence of the foam impact is expected from radiative transfer models of foam emissivity at L-band in the range 0°–50° [Reul and Chapron, 2003; Camps et al., 2005; Yueh et al., 2010], a characteristic which was confirmed in the observations over IGOR (Reul et al., 2012). Surface wind speed modulus is finally retrieved from ΔI data using the bi-linear GMF proposed in Reul et al. 2012.

2.2 Storm Tracks and Intensity

Tropical cyclone best track data were obtained from the WMO official archiving and distribution resource IBTrACS: International Best Track Archive for Climate Stewardship (Knapp et al. 2010). We used the best track archive dataset version v03r06 available at NOAA National Climatic Data Center (https://www.ncdc.noaa.gov/ibtracs/). The database include 6-hourly eye track location and maximum 1-minutes sustained wind speed information. We used the "source" datasets in the Best track data which combines information from the most reliable tropical cyclone data centers. At the time this work was conducted, the IBTrACS tracks database only included few storms in 2014 and none in 2015. For this two years, we completed the storm track database using data from the Joint Typhoon Warning Center (JTWC) or National Hurricane Center (NHC).

The position of the storm center at the time of SMOS acquisition was determined from time interpolated best track data but also using microwave 85 GHz data from SSMI15-16-17-18, TMI and AMSRE. The latter data are available from the Morphed Integrated Microwave Imagery (MIMIC-TC) database provided by the Cooperative Institute for Meteorological Satellite Studies Space Science (CIMSS). By default, we used the Best Track interpolated eye location at the time of SMOS overpasses. However, adjustments were performed if a visual inspection revealed discrepancy between the best tracks interpolated eye location, the 85 GHz and the SMOS fields (e.g., cases when the eye is very easily detectable on SMOS data by visual inspection but displaced from best track or 85 GHz's estimates).

The bearing of the storm eye main motion at SMOS acquisition time was also estimated from the time interpolated 6-hourly best-track data.

2.3 Surface wind speed products

SMOS data and retrieved winds are compared in that paper with an ensemble of surface wind speed products to provide validation datasets and to compare the performances of SMOS retrievals with respect other wind estimates such as Numerical Weather products and ocean surface winds from the ESA MetOp-A and B Advanced Scatterometer (ASCAT).

For Validation, we specifically used retrieved surface winds from either the SFMR aboard the C-130 aircraft or H*WIND analyses (Powell et al., 1998). Both data are available from the Hurricane Research Division (HRD) of the Atlantic Oceanographic and Meteorological Laboratory.

The SFMR was specifically developed to measure hurricane-force ocean surface winds. Thus, the instrument has been mounted on aircraft that typically make butterfly-pattern reconnaissance flights within TCs. In general, SFMR measures the nadir brightness temperatures between 4.5 and 7.2 GHz, which are converted to 1-minute sustained surface wind speeds and rain rates using dedicated GMF. SFMR data are provided at a high radial resolution of ~3km. Comparison of SFMR to GPS dropsonde wind speed measurements resulted in an error of approximately 4 m s^{-1} in TC winds between 10 and 70 m s^{-1} (Uhlhorn et al., 2007).

To validate and re-analyse the SMOS GMF, we also used H*WIND two-dimensional surface wind analysis products [Powell et al., 1998]. The H*wind analysis uses a combination of all available surface and near surface wind observations collected over several hours period from multiple platforms (i.e., SFMR wind speeds, GPS dropwindsondes, tail Doppler radar, geostationary operational environmental satellite (GIES) cloud track winds, surface ships and buoy data as well as satellite observations (such as QuicSCAT, WindSat and ASCAT), etc.), adjusts them to a common elevation and exposure to create a 6 km resolution tropical cyclone surface wind field given into a "storm-centric" moving TC coordinates system. The wind speed represents the one-minute sustained wind velocity at 10-m altitude reference.

These objectively analyzed wind products are used routinely as guidance for operational TC forecast and advisory products, including the determination of wind radii (e.g., radius of 17, 25, and 33 m s-1 winds by quadrant) by hurricane forecasters at the National Hurricane Center and the Central Pacific Hurricane Center. H*wind accuracy is highly dependent on the quality of the dataset and data coverage used as input. Although it is imperfect, it is the current best 2D surface truth available. Note that these fields are only freely available until 2013.

Prior to making comparisons with SMOS data, all SFMR and H*wind measurements are corrected for the time difference between SMOS acquisition and the flight track. Therefore, every measurement is shifted with respect to the movement of the storm centre within the time difference. This results in adjusted flight tracks such that SFMR and H*WIND measurements have the same location with respect to the centre of the storm during the SMOS acquisition as they actually had when they were recorded. This adjustment does not consider any storm rotation. The storm's movement is derived from the best track information from IBtracks. We considered all SFMR and H*WIND observations available within ±12 hours from SMOS data. The two closest H*WIND wind fields in time (before and after a SMOS overpass of storms) available within that window were linearly interpolated at the SMOS acquisition time. Both SFMR and H*WIND products were kept at their original spatial resolution but smoothed at SMOS averaged spatial resolution of ~43 km by using a running Gaussian windows.

Note that Hurricane surface winds are strongly dependent on the averaging time attributed to the wind observations, the roughness of the underlying surface, and height of the wind measurements. The NHC best track maximum sustained surface wind is defined as the maximum 1-min wind that might be observed at a height of 10 m. Here, all the other wind products are also referred to the 10 m height. The H*WIND averaging time is also 1 min, so that the SMOS retrieved wind speeds, by construction of the GMF derived in Reul et al., 2012, were calibrated based on a 1 min averaging period. However, SMOS spatial resolution is at best ~30 km at nadir, and most of world's operational centers outside of the U.S. consider the intensity to be defined by the maximum 10-min wind, which may be more consistent with the spatial resolution of SMOS. Therefore, all wind speed value derived based on a 1 min averaging period were adjusted to the 10-min standard. The relation of 1-minute to 10-minute averaged wind speed is that the latter is 7% smaller (Harper et al., 2010).

The European Centre for Medium-range Weather Forecasts (ECMWF) 10-m equivalent neutral wind data are used as auxiliary information in the SMOS operational Level 2 processing to improve the Sea Surface Salinity (SSS) retrievals. We therefore also considered the use of those ECMWF 3 hourly 25 km products interpolated at 15 km and at SMOS acquisition time but also of the 6-hourly GFS NCEP wind speed products for comparison with reference datasets (SFMR or H*WIND). The NWP winds were co-localized in space and linearly interpolated in time with SMOS acquisition.

2.4 Rain data

Satellite rain rate estimates that we used in the present products are the CMORPH products (CPC MORPHing technique) which include global precipitation analyses at high spatial (~8km) and temporal resolution (~3 hourly). This technique (Joyce et al., 2004) uses precipitation estimates that have been derived from low orbiter satellite microwave observations exclusively, and whose features are transported via spatial propagation information that is obtained entirely from geostationary satellite IR data. At present NOAA incorporate precipitation estimates derived from the passive microwaves aboard the DMSP 13, 14 & 15 (SSM/I), the NOAA-15, 16, 17 & 18 (AMSU-B), and AMSR-E and TMI aboard NASA's Aqua, TRMM and GPM spacecraft, respectively. IR data are used as a means to transport the microwave-derived precipitation features during periods when microwave data are not available at a location. Propagation vector matrices are produced by computing spatial lag correlations on successive images of geostationary satellite IR which are then used to propagate the microwave derived precipitation estimates. This process governs the movement of the precipitation features only. At a given location, the shape and intensity of the precipitation features in the intervening half hour periods between microwave scans are determined by performing a time-weighting interpolation between microwave-derived features that have been propagated forward in time from the previous microwave observation and those that have been propagated backward in time from the following microwave scan. NOAA refer to this latter step as "morphing" of the features. CMORPH estimates cover a global belt (−180°W to 180° E) extending from 60°S to 60°N latitude and are available at ftp://ftp.cpc.ncep.noaa.gov/precip/CMORPH_V1.0/RAW/

With regard to spatial resolution, although the precipitation estimates are available on a grid with a spacing of 8 km (at the equator), the resolution of the individual satellite-derived estimates is coarser than that - more on the order of 12 x 15 km or so. The finer "resolution" is obtained via interpolation. Similarly to the wind speed products, we estimated the rain rate on the SMOS 15km resolution grid by averaging the CMORPH data using a 2D gaussian windows of 43 km width. The two closest CMORPH fields in time (before and after a SMOS overpass of storms) were linearly interpolated at the SMOS acquisition time.

2.5 Altimeter and ASCAT data

Altimeter data come from the Jason-1 and Jason 2 Geophysical Data Records (GDR) and ASCAT A & B data are level 2B products available at Ifremer/CERSAT satellite data center (http://cersat.ifremer.fr/). Altimeter Data have been edited to eliminate measurements contaminated by rain by the standard Jason-1& 2 rain flags, by radiometer liquid water content exceeding 0.2 kg m^{-2} and by using the Ku-band versus C-band radar cross section relationships (see Quilfen et al., 2011).

3 SMOS STORM Database

3.1 General Characteristics of the SMOS STORM database and analysis subset

A database of SMOS interceptions with Tropical Cyclones has been generated for the satellite data archive period from January 2010 to April 2015 and will be referred hereafter as the "SMOS-STORM database". SMOS intercepts with all TCs were determined for each storm of the track database by selecting SMOS swaths that intercepted the storm tracks while including the storm center location. For each swath, the SMOS L1B data were processed to estimate the residual half-power first Stokes radio-brightness contrasts at surface level on the 15 km grid. The SMOS retrieved 2D wind speed modulus fields based on the first GMF (Reul et al., 2012) were evaluated and collected with a suite of auxiliary geophysical information (ECMWF, NCEP wind and SST, SSS from SMOS Level 3, etc..). The intercepting swaths were then classified by year, basin and storm names and the data were saved as netcdf files.

A sub-ensemble of about 300 SMOS swath intercepts with Tropical storms and cyclones (among the total database) has been further selected. These data were selected based on how well the swaths intercepted the storms in their centers (the storm center and its spatial domain within a radius of ~100-200 km had to be well observed by the instrument). The selection was also done based on the general SMOS data quality within each swath (minimum RFI contaminations and undetectable residual uncorrected solar effects..). These data of the highest quality possible were selected to properly estimate the geophysical dependencies of the L-band contrasts in storms and to learn more about how the data shall be physically interpreted and inverted into geophysical parameters (wind, wave, rain,etc..).

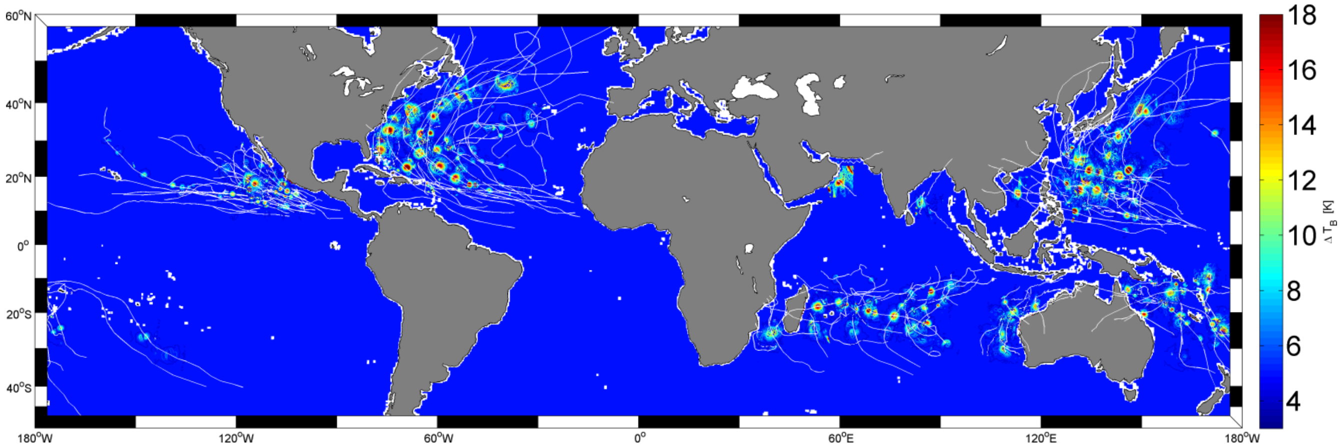

Figure 1: Global distribution of the Storm-induced L-band radio brightness contrasts for an ensemble of SMOS intercepts with Tropical Cyclones over 2010-2015.

The global distribution of the L-band brightness contrast intensity associated with that sub ensemble of intercepts is shown in Figure 1. Focus on the superimposed brightness temperature contrasts (in terms of contours of ΔI) for each major TC zones are provided in figure 2. As shown, we selected storms in almost all of active basins of the world oceans showing an important variability in the brightness temperature contrasts distribution for each basin.

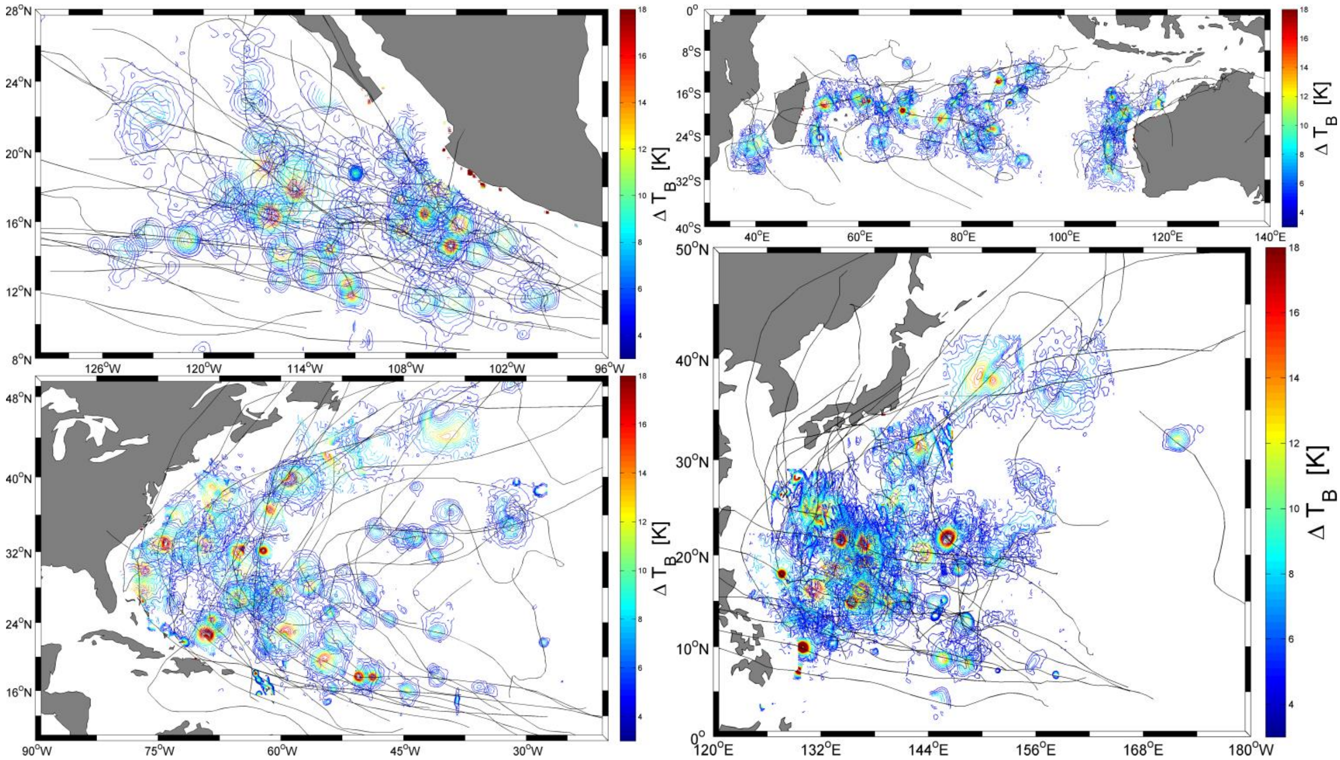

Figure 2: Contours of the selected storm-surface induced brightness temperature contrasts [K] as estimated from SMOS L-band data for an ensemble of storms in the Eastern Tropical Pacific (Top left), North Atlantic (Bottom left), Southern Indian Ocean (top right) and Western Pacific ocean (bottom right) during 2010-2015. The black thin curves indicate the storm tracks. The color indicate the amplitude of the storm-induced radio-brightness temperature contrasts.

In figure 3, we further show several representative examples of the brightness temperature contrasts estimated from SMOS data as the instrument intercepted some storms with intensity ranging from Tropical Storms to category 4 on the SSHWS. As shown, the shape, magnitude and spatial extent of the storm-induced L-band brightness temperature contrasts are showing significant variability around the storm centers. Large asymmetries in the distribution of the ΔI around the eyes are particularly evident for the tropical storms and category 1-2 TCs. The magnitude of the maximum storm-induced signal is also varying from below 12 K for Tropical storms to well above 18 K for Category 4 cyclones and can be found distributed on different sides of the storm tracks. Significant drops of ΔI in the eye center regions, known to be associated with light winds and low rain, are very often visible in the images but not systematically observed, particularly for those storms showing radii of significant ΔI contrasts which are on the order of, or less than, the instrument average spatial resolution (~43 km).

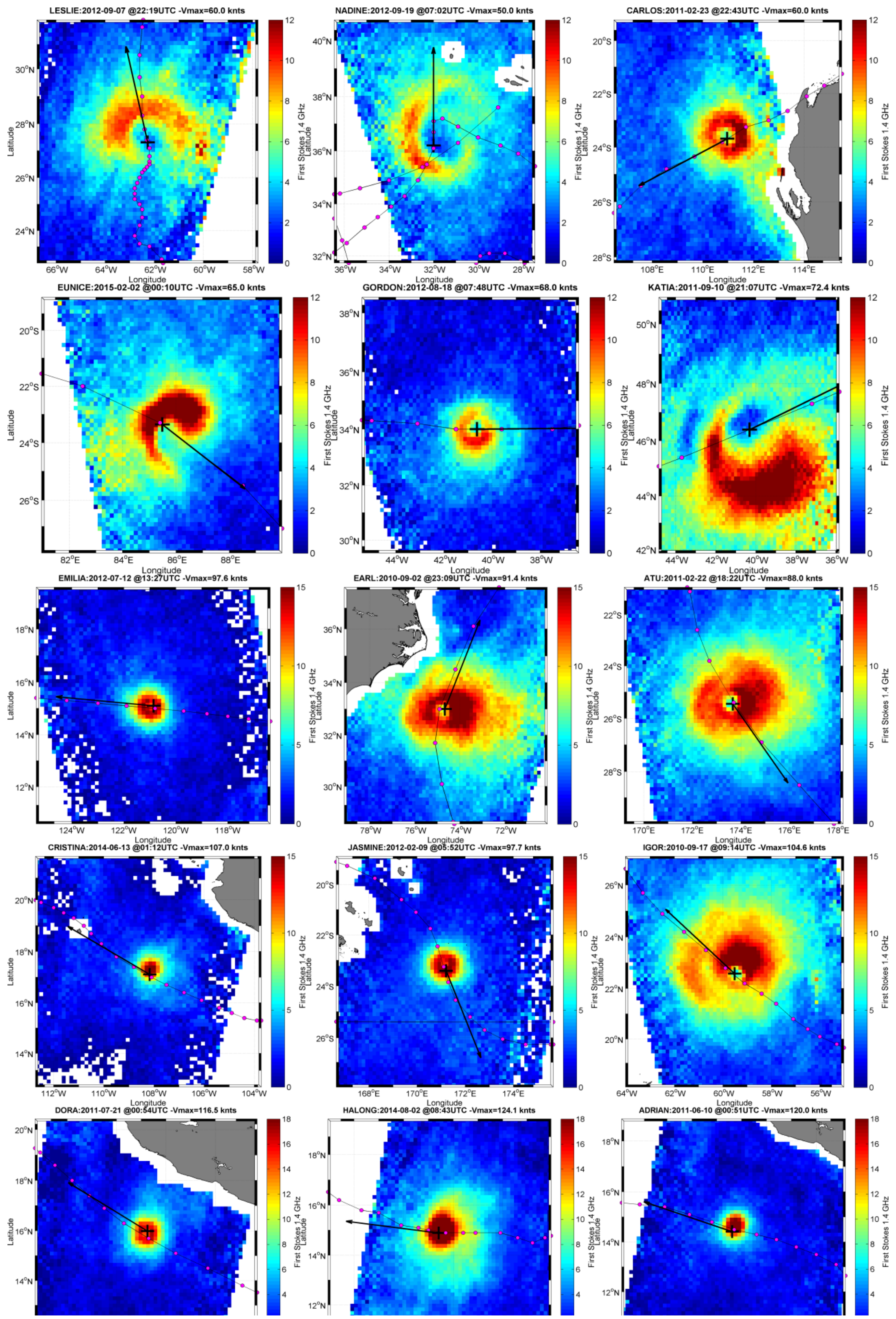

Figure 3: Examples of L-band radio-brightness temperature contrasts [K] measured by SMOS as the instrument intercepted Tropical Storms (upper-panel, 35-63kts), category 1 TC (second panels from top, 64-82knts), category2 TCs (third panels from top, 83-95 knts), category 3 TCs (fourth panels from top) and category 4 TCs (bottom panels). Note that the color-scale range is 0-12 K for TS and category 1, 0-15 K for category 2 to 3 and 0-18 K for category 4 on the SSHWS. Each panel represent a domain of about 1000 km width centered on the TC eye. The pink dots show the storm 6-hourly best track and the black arrow indicate the storm main propagation direction.

The selected subset of SMOS intercepts has been further classified as function of the value of the best track 10mn maximum sustained wind speed at the time of SMOS acquisitions to finally include intercepts with 124 tropical storms, 74 category 1, 41 category 2, 36 category 3, 22 category 4 and 3 category 5 events.

3.2 Statistical characteristics of the L-band brightness contrasts as function of storm intensity and sectors

3.2.1 Transformation of ΔI into Storm-centric and common propagation direction frame

To estimate the 'average' statistical properties of the brightness temperature contrasts and their dependencies with storm intensity and storm sectors, each SMOS intercept with a storm was processed as follows:

1) The storm center was determined at the time of SMOS acquisition by interpolating linearly in space and time the storm track 6-hourly IBTracks data at the SMOS acquisition time,

2) Microwave 85 GHz data from SSMI15-16-17-18, TMI or AMSRE that were acquired within less than ±1 hour apart from SMOS intercepts were further used to check the determination of the storm center locations estimated from the best-track data. If 85 GHz images were available within less than ±half an hour from SMOS, the location of the center determined by CCIMS from these high microwave frequency images was used. Otherwise, the center location was bi-linearly interpolated in space and time from the two closest 85 GHz observations acquired just before and after SMOS acquisition. A visual check was further performed to check consistency between SMOS eye location, best-track and 85 GHz interpolated ones. In case of mismatch, the center determined from the 85 GHz data was used by default. An example is shown in Figure 4 for a SMOS intercept of the hurricane JOVA as it developed in the eastern Pacific into a Category 3 storm, on 10 october 2011, before it landed in western Mexican coasts. SMOS intercepted the storm at 12:32 Z. The best-track linearly-interpolated eye location at that hour (see Figure 4, top left panel) is found at ~[16.5°N, 106.8°W] which is about 0.5° north of the observed maximum in SMOS brightness temperature contrast. If the best-track determined eye location is assumed to

be the actual storm center, then SMOS ΔI distribution as observed would be strongly asymmetric with a significant right-hand displacement of the maximum brightness contrast with respect the storm track. An 85 GHz image from SSMIS-17, available 28 minutes away from the SMOS data, however reveals that the storm eye was actually centered at [15.8°N, 106.78°N], consistent with the centroid of SMOS ΔI observations. This example illustrates the need for a very careful inspection and determination of storm eye centers, if one want to estimate the actual statistical properties of the brightness temperature in a storm-centric frame and determine potential asymmetries around the different storm sectors.

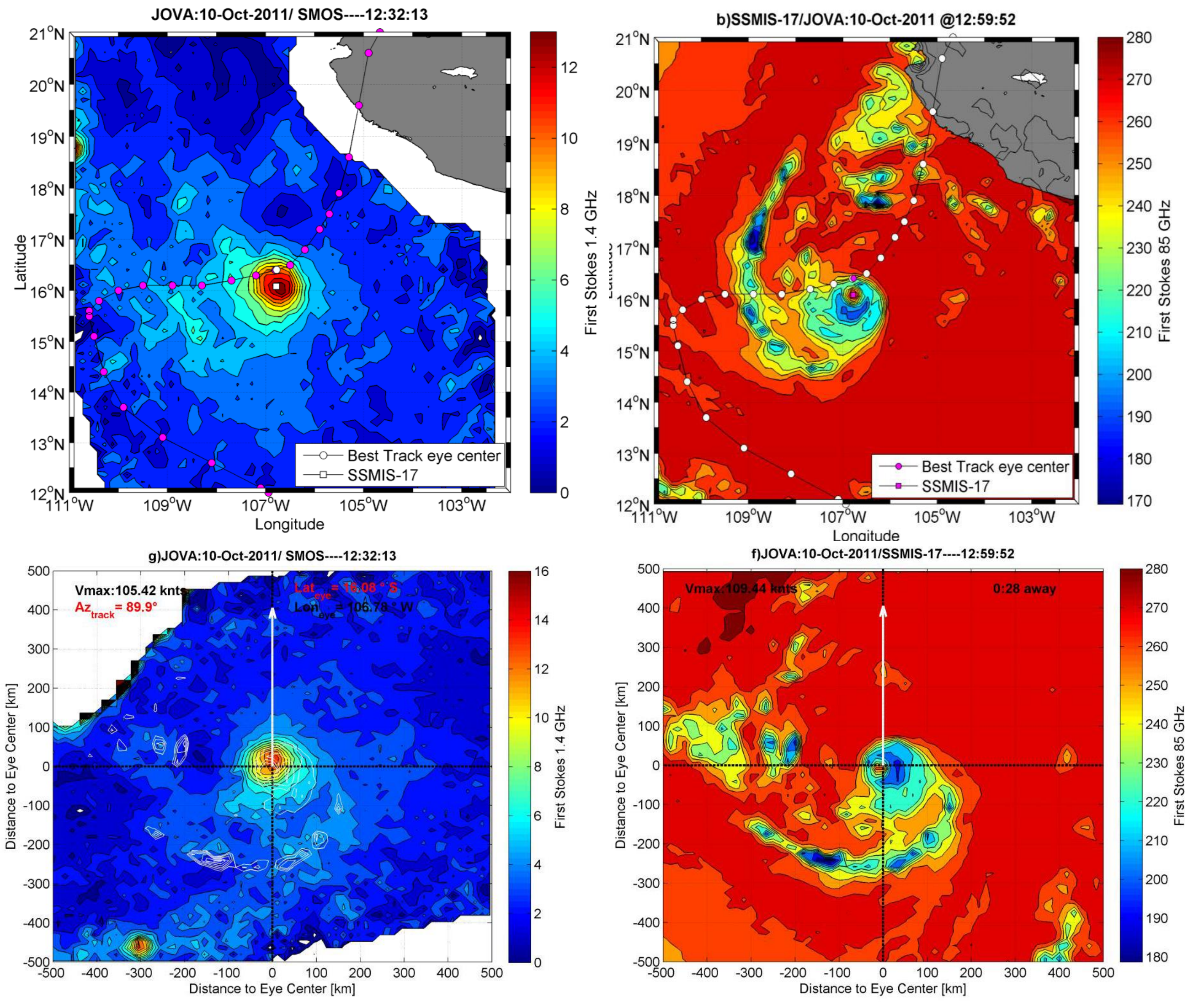

Figure 4: Top left : SMOS radio-brightness contrast estimated over Category 3 TC JOVA at 12:32 Z on 10 october 2011. The pink dotted curve indicate the best track of JOVA; the white filled dot and squares indicate the eye location estimated by linear interpolation of the best track data at SMOS acquisition time and from the closest 85 GHz acquisitions, respectively. The latter is obtained from SSMIS/17 imagery at 12:59 Z (Top right). Bottom panels: same fields than top panels but provided in a storm-centric frame of 1000 km^2 and rotated with respect the storm heading (white arrow).

Once the storm eye locations were best estimated at the SMOS acquisition times using the previous methodology, all ΔI data were further re-gridded at 15 km resolution on a storm-centric coordinate system with west-east and north-south axes spanning a spatial domain of 500 kms on each sides of the storm centers. In addition, the heading of the storm translation motion was estimated from the best-track interpolated data at SMOS acquisition time and the brightness contrasts fields were further rotated to align all storm center translation directions to a common axis, here arbitrarily chosen to be due North (see example for JOVA in Figure 4, which was heading towards the east at SMOS acquisition time). Note that an additional 180° rotation around that axis was applied to the fields for the southern-hemisphere storms to account for the differing veering wind directions on both hemisphere, so that the ΔI distributions are all given in a "northern-hemisphere" common coordinate system.

3.2.2 Statistical distributions of ΔI as function of storm intensity and sectors

The 2D distributions of the mean and standard deviation of the L-band storm-induced brightness temperature contrasts as function of the different categories of storm intensity on the SSHWS are given in Figure 5.

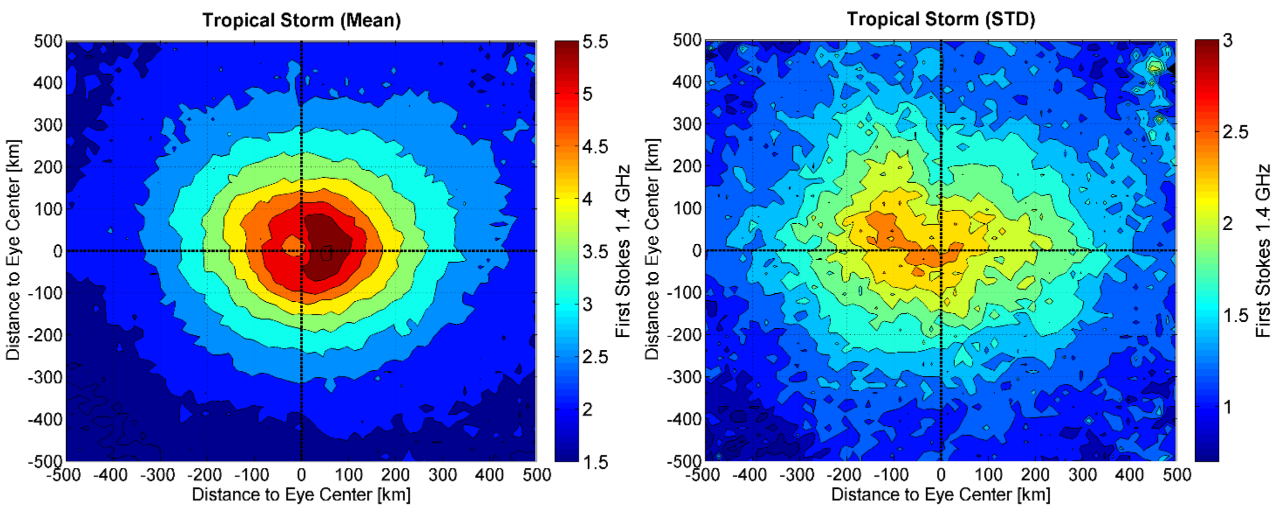

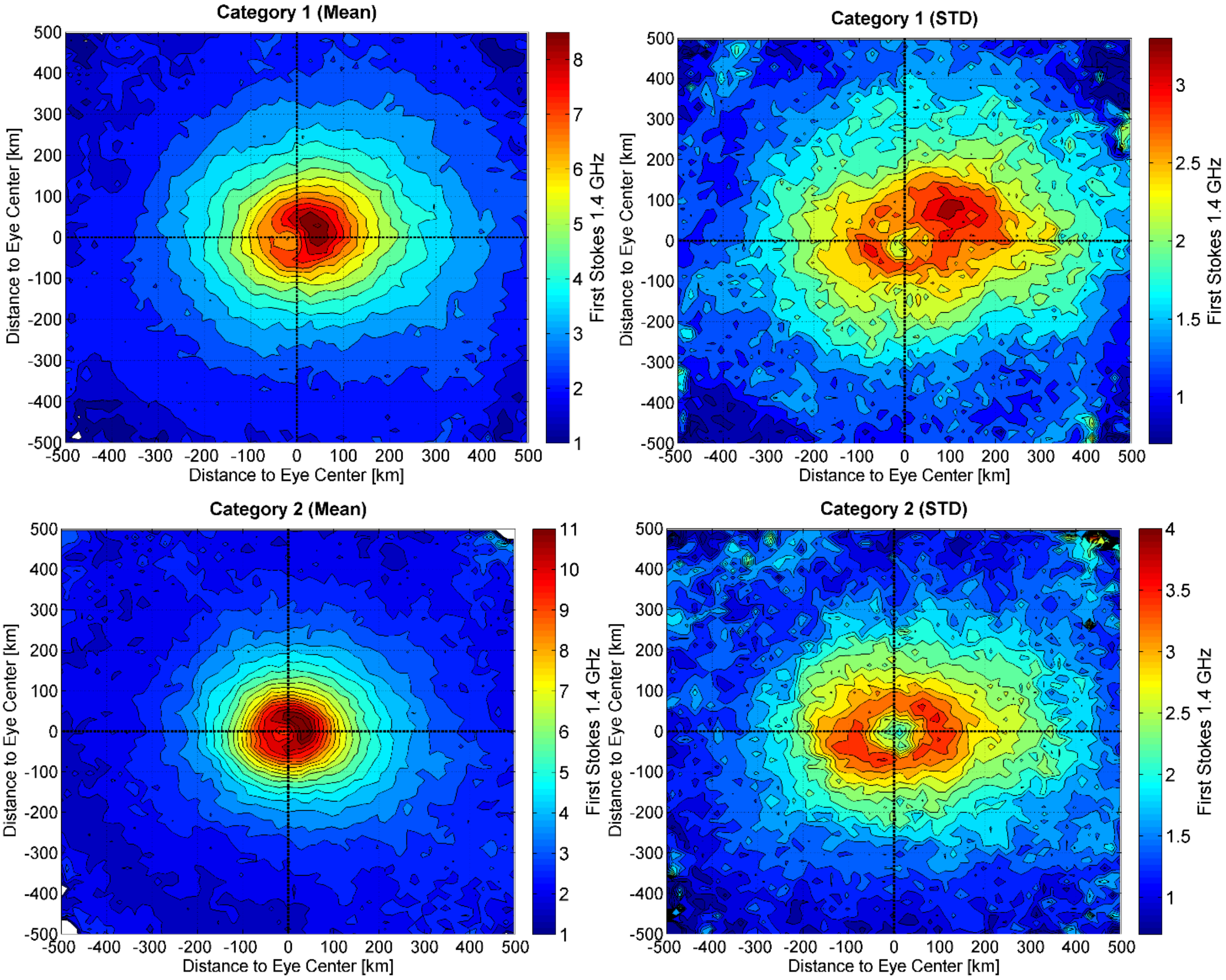

(see legend and rest of the figure next page)

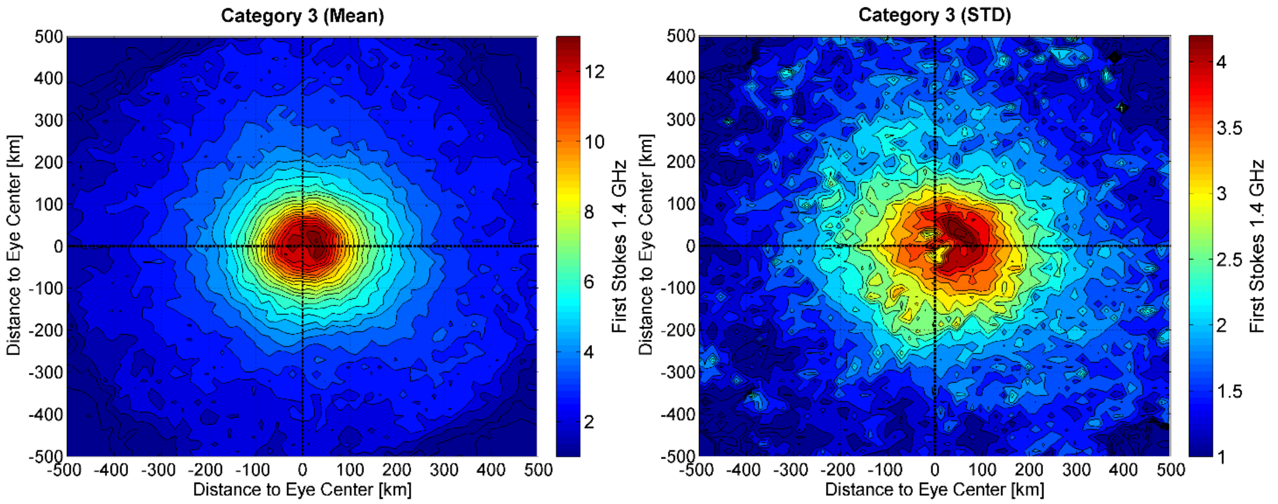

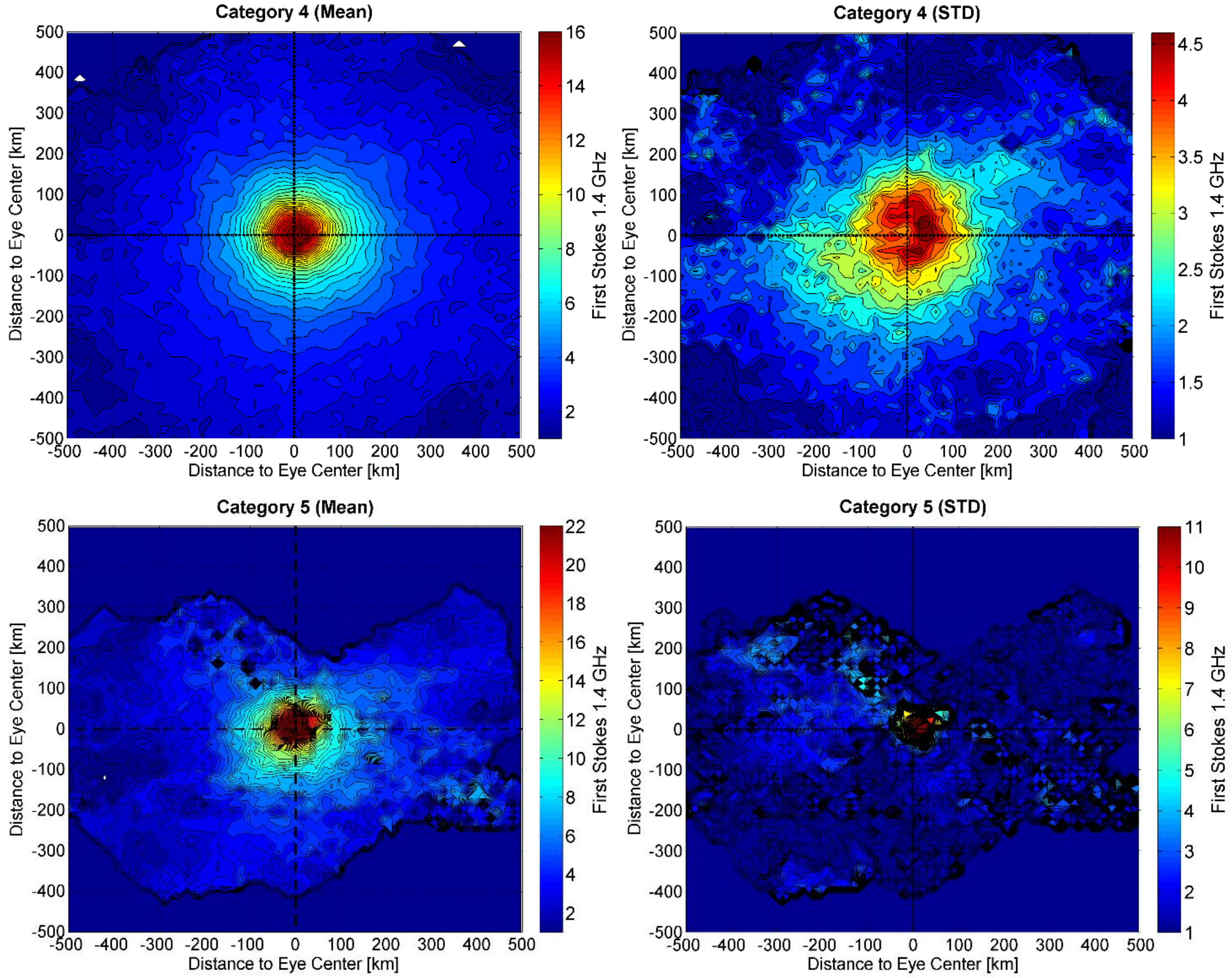

Figure 5: Storm centric contours of the mean (left panels) and standard deviation (right panels) of the L-band radio brightness half power contrast as function of storm sectors and intensity. The wind intensity is ranging from Tropical storms (Top panels, $35 \leq U_{10} \leq 63$ kts), Category 1 TCs (second panels from top, $64 \leq U_{10} \leq 82$ kts), Category 2 TCs (3rd panels from top, $83 \leq U_{10} \leq 95$ kts), Category 3 TCs (4th panels from top, $96 \leq U_{10} \leq 113$ kts), Category 4 TCs (5th panels from top, $114 \leq U_{10} \leq 135$ kts) and Category 5 (bottom panels, $U_{10} > 135$ kts). Contours are ranging from 1 to 28 K per steps of 0.5 K for the mean and from 0 to 10K per steps of 0.2 K for the standard deviation. Note that the color scale range is changing from top to bottom panels.

As shown, the averaged distributions of ΔI reveal that the mean brightness contrast amplitude is coherently increasing with the increasing intensity of TCs. The radii within which the brightest ΔI values are found for each category is also seen to diminish as the storm intensity increases, consistent with the reported evolution of the highest surface wind distribution in TCs (Holland, 1980). A remarkable feature of the mean ΔI fields is that the maxima of ΔI are systematically found on the right-hand sides quadrants of the storms. Here again, this is consistent with the reported asymmetric structure of the wind and wave fields in hurricane, with the maximum in wind speed and sea surface heights occurring in the right-hand quadrants of the storms (in the northern-hemisphere) because of the relative wind created by a translating storm. Except for the tropical storm intensities, the standard deviation (STD) of the ∆I fields also reflect the mean field characteristics. For categories 1-5, the STD is showing a quasi-annular distribution around the storm center, with local minima at the center, a signature of the relatively calm eye of the TCs and local maxima in the right-hand quadrant of the storms.

These statistical features of the L-band brightness temperature contrasts in storms are further illustrated in Figure 6 where we show the storm quadrant azimuthally-averaged radial distributions of the ∆I fields. RHS quadrant asymmetries in the maxima of ∆I (always found in the north-east & south-east quadrants) are very clearly evidenced. Likely because the averaged radii of maximum wind drops below ~50 km for storm intensities above and including category 4 on the SSHWS, the instrument hardly resolves the TC eye structures for those most intense storms.

Figure 7 summarizes the storm quadrant and intensity dependencies of the L-band half-power radio-brightness contrasts in tropical cyclones. As clearly evidenced, the mean brightness contrast is monotonically increasing with storm intensities within a ~200 km radius from the storm center. The mean ∆I amplitude thus ranges from about 5K for tropical storms up to ~22K for the most intense category 5 cyclones. No saturation in the ∆I is visible above hurricane force and the brightness increase from one category to the other on the SSHWS is generally on the order of 3-4 K. The step change from Category 4 to Category 5 is more significant (~8 K) but this result shall be taken with caution given that only 3 Category 5 events were intercepted by SMOS and hence used to derive the statistics.

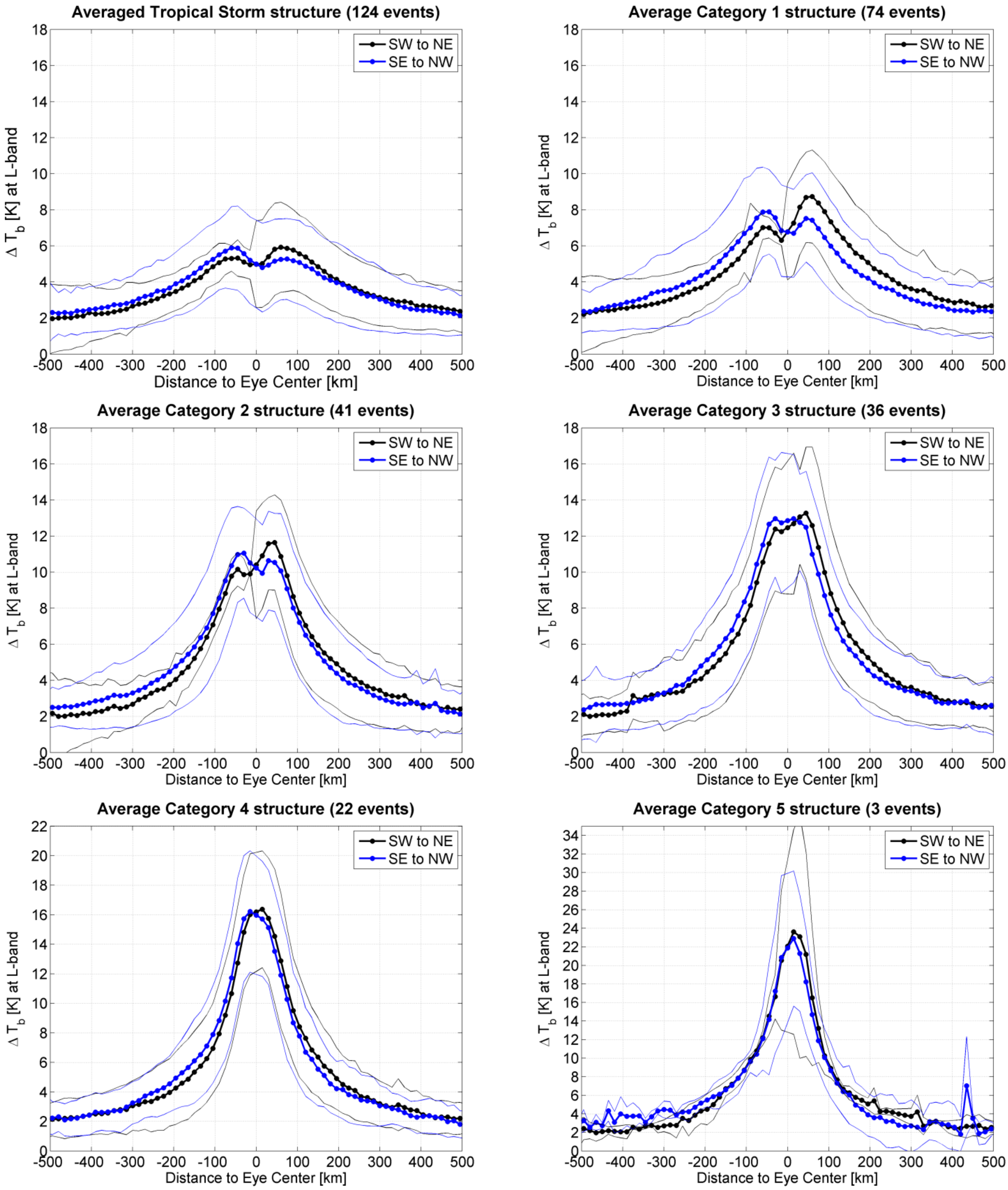

Figure 6: Mean radial distribution of the L-band wind-excess brightness temperature per storm quadrants and for each category of storm intensities on the Saffir-Simpson scales. Thick black and blue dotted curves indicate the mean radial distribution of ΔI from the South West to the North East storm quadrants, and from the South East to the North West storm quadrants, respectively. The thin curves indicate the corresponding mean±1 standard deviation for each quadrant. Top left: Tropical storm intensity. Top right: Category 1 storms. Middle left: Category 2 storms. Middle right: Category 3 storms. Bottom: Category 4 (left) and 5 (right). Note that the Y-axis range is not necessarily constant from one panel to the other.

4

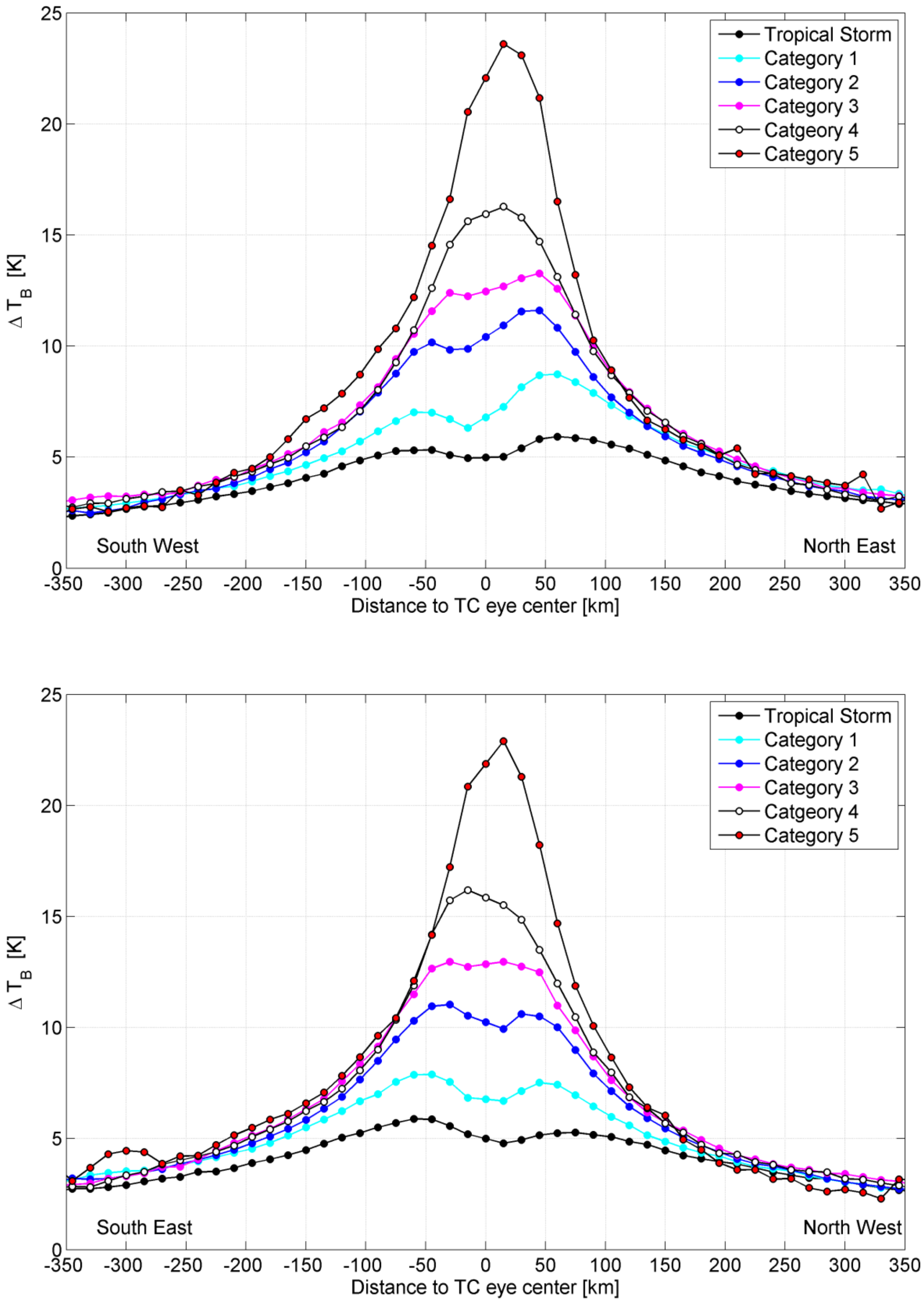

Figure 7: Mean radial distribution of the storm-induced L-band half-power radio-brightness contrasts ΔI from the South West to the North East storm quadrants (top), and from the South East to the North West storm quadrants (bottom) as function of storm intensities (colors) given by the SSHWS.

5 A revised L-band Geophysical Model Function

The bi-linear GMF relationship between ΔI and the 10 m height surface wind speed U_{10} proposed in Reul et al., 2012 has been inferred solely from observations acquired over a single north-Atlantic hurricane event (Category 4 hurricane IGOR in 2010). A revision of that GMF is provided here below successively using co-localized SMOS, SMFR flight track data and analysed 2D H*Wind fields.

5.1 Systematic comparisons between SMOS and SFMR

Considering the SMOS-STORM database, we found 64 co-localized SMOS swath intercepting SFMR flight tracks in ~30 TCs over the period 2010-2014. This SMOS-SFMR match-up database was built up by selecting co-localized data with time differences between both acquisitions less than ±10 hours. If the central time lag Δt between SMOS and SFMR data as the aircraft flew over the eye regions exceeded ±half an hour; the storm center displacement between the aircraft and satellite acquisitions could have been significant. To correct for the storm motions when |Δt |>0.5 h, SFMR tracks were spatially translated (without rotation) from the original eye location detected in SFMR data to the eye location at the SMOS time. The SMOS brightness contrasts were then further bi-linearly interpolated in space at ~6km high resolution along each flight track.

The distribution of the ensemble of co-localized SMOS and SFMR flight tracks is provided in Figure 8.

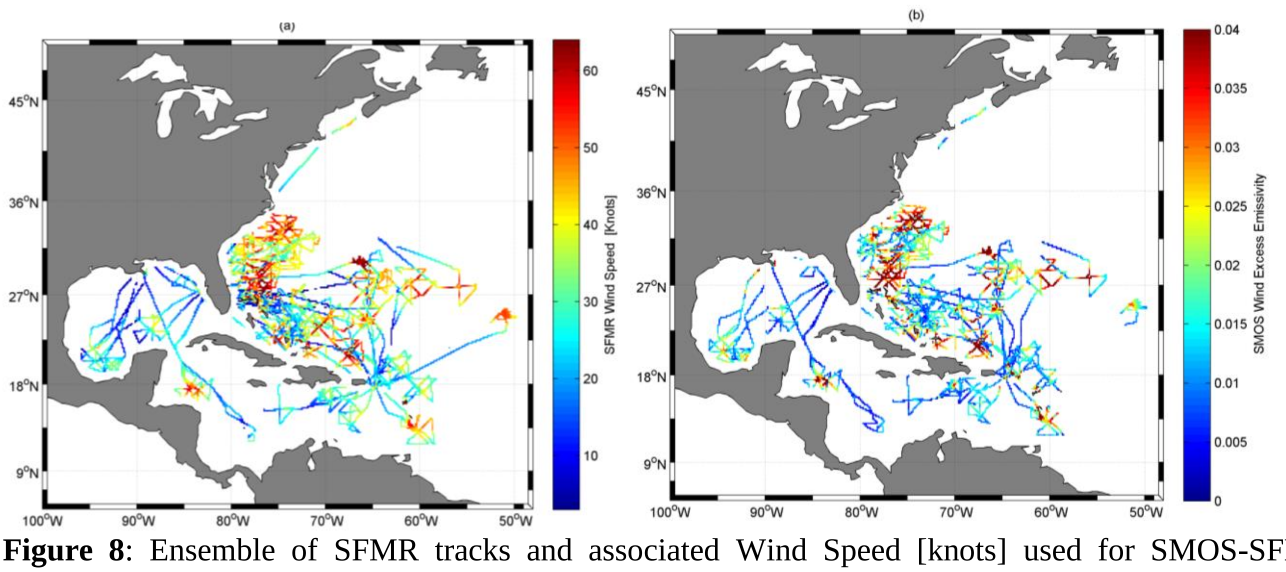

Figure 8: Ensemble of SFMR tracks and associated Wind Speed [knots] used for SMOS-SFMR comparisons (left) and SMOS L-band excess emissivity contrasts co-localized with SFMR flights.

As shown, these data include only intercepts with storms that developed in the North-Atlantic and Gulf of Mexico. Given the varying sea surface temperature (sst) conditions possibly encountered for all the storms, in what follows, the radio-brightness contrast estimated from SMOS will be now expressed in terms of the storm wind-excess emissivity: $\Delta e=\Delta I/sst$. As seen in Figure 8, the relative distribution of wind speed measured by SFMR closely match the one of the co-localized SMOS Δe, with brightest spots in SMOS data almost always spatially coincident with the highest wind regions retrieved along SMFR flights.

In figures 9-12, we show representative examples of the co-localized surface wind speed retrieved from SMOS using the first GMF (Reul et al., 2012) compared to SFMR estimates. Note that SFMR high resolution Surface Wind Speed (SWS) data were also spatially averaged along their track using a Gaussian running window of ~30 km width, the highest spatial resolution of SMOS multi-angular pixels. Both spatially filtered and nominal resolution data are shown for comparisons. As shown in these examples, SMOS estimate well reproduce in general the SFMR surface wind speed observations. The match is particularly good in the highest wind speed range although high wind gradients regions and high spatial-resolution variability around the TCs eyes are often smoothed out by the low spatial resolution of the SMOS instrument, as also observed in the spatially smoothed SMFR data. Mismatches and biases are nevertheless also often detected in the intermediate wind speed range from 15 to 30 m/s independently of the time lags between SMOS and SFMR.

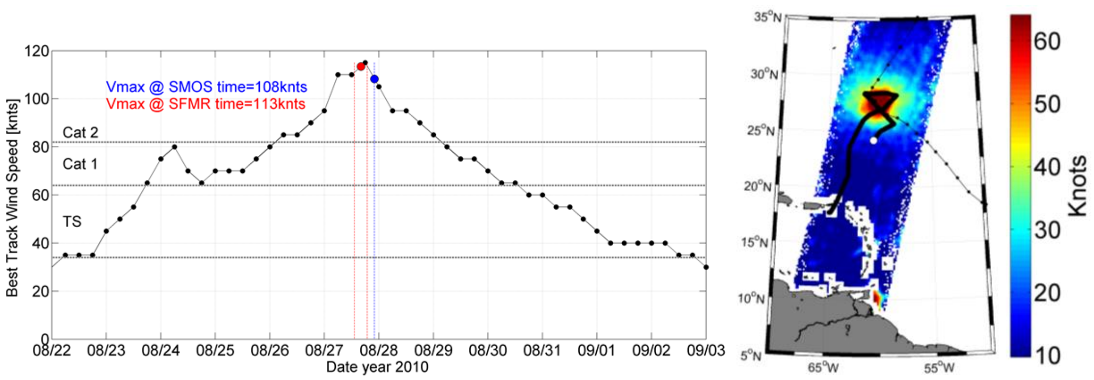

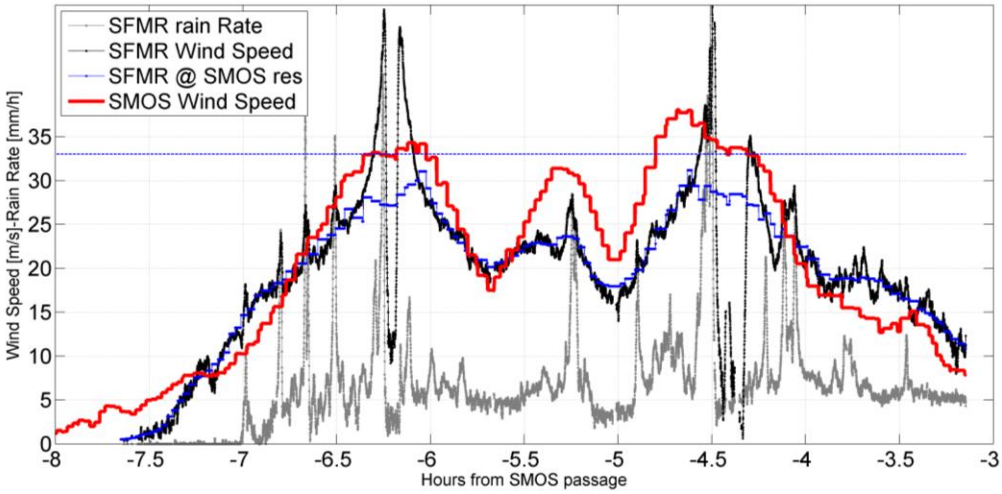

Figure 9: Top left: Time series of the best track maximum sustained wind speed for hurricane Danielle in 2010 with time of intercept from SFMR (red dot) and SMOS (blue dot). Top right: superimposed SMOS retrieved wind speed using the first GMF (color in knots) and SFMR track (black thick curve). The thin dotted curve indicate the storm track. Bottom: time series of the SFMR retrieved wind speed in m/s (black curve) and rain rate in mm/h (grey curve) at nominal resolution along aircraft track (~6 km). The SFMR retrieved wind speed spatially averaged with a running window of 30 km width along track (corresponding to the highest resolution of SMOS interferometer pixels) is shown in blue. The retrieved wind speed from SMOS is shown in red. The x-axis shows the time lag between SFMR acquisitions and SMOS ones.

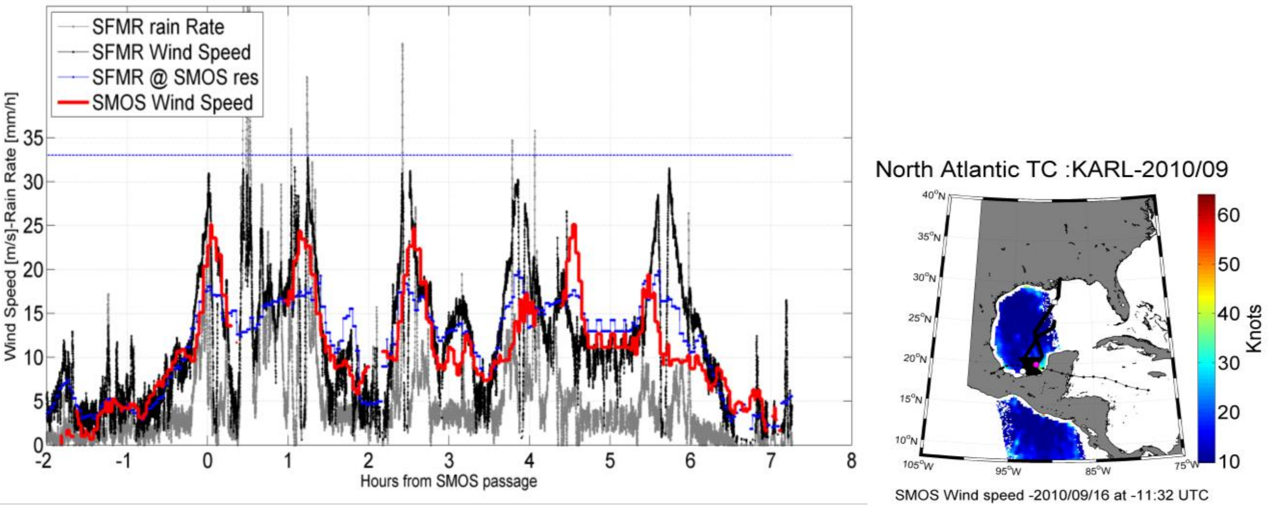

Figure 10: Top: Swath of SMOS retrieved wind sped using first GMF as the instrument intercepted Hurricane Karl on 16 september 2010 as it reached Category 1 intensity. The black curve indicates the track of the aircraft carrying the SFMR. The thin blue line is the storm track. Bottom: time series of the SFMR and SMOS data along the track. The time is centered relative to the SMOS acquisition time. The black curve shows the SFMR retrieved wind speed at original resolution ~3 km. The blue curve shows the SFMR retrieved wind speed smoothed at 43 km resolution along track. The red curve shows the SMOS retrieved wind speed co-localized along the aircraft track. The gray curve shows the SFMR retrieved rain rate.

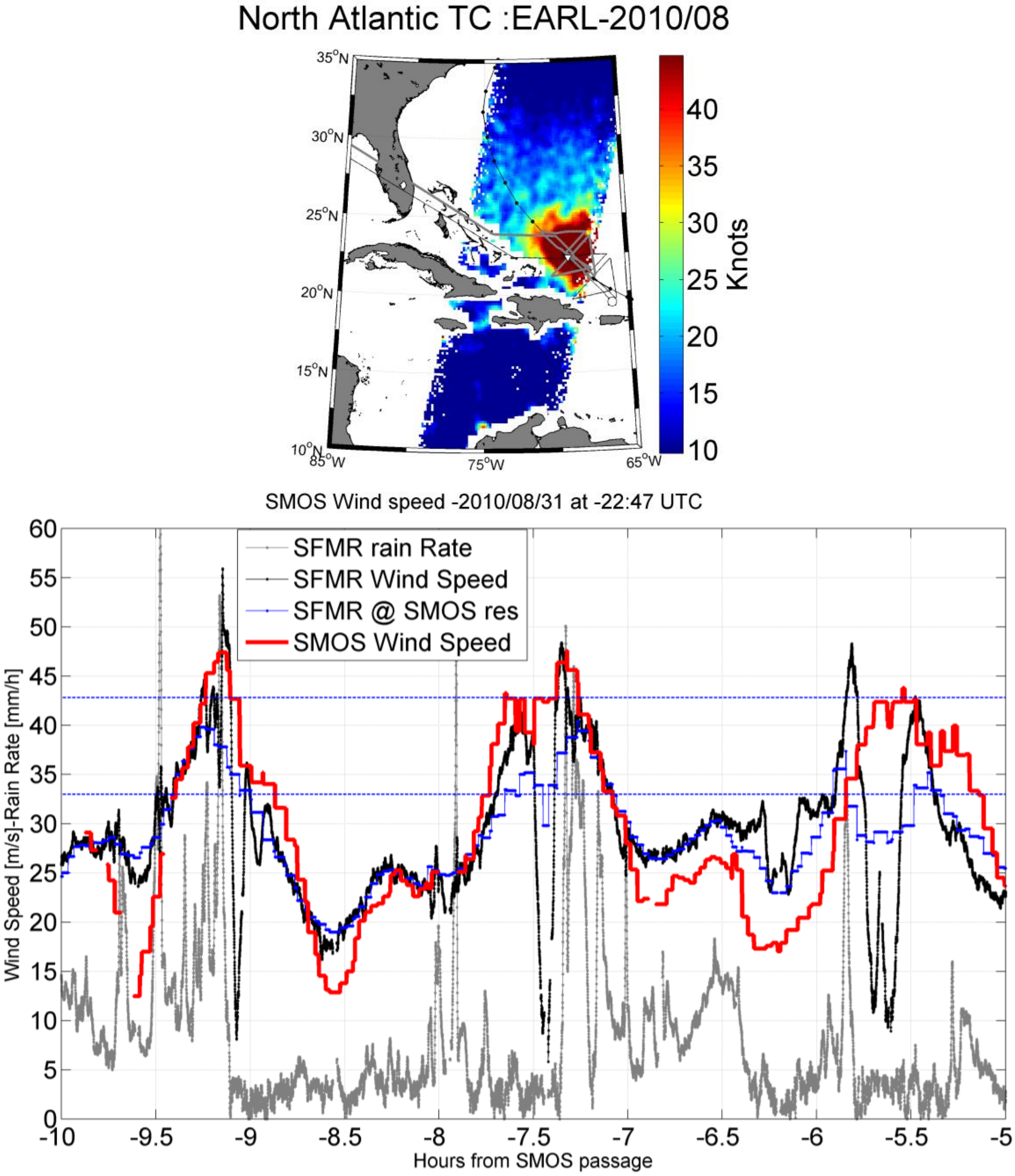

Figure 11: Idem than Figure 10 but for Hurricane Earl on 31 August 2010.

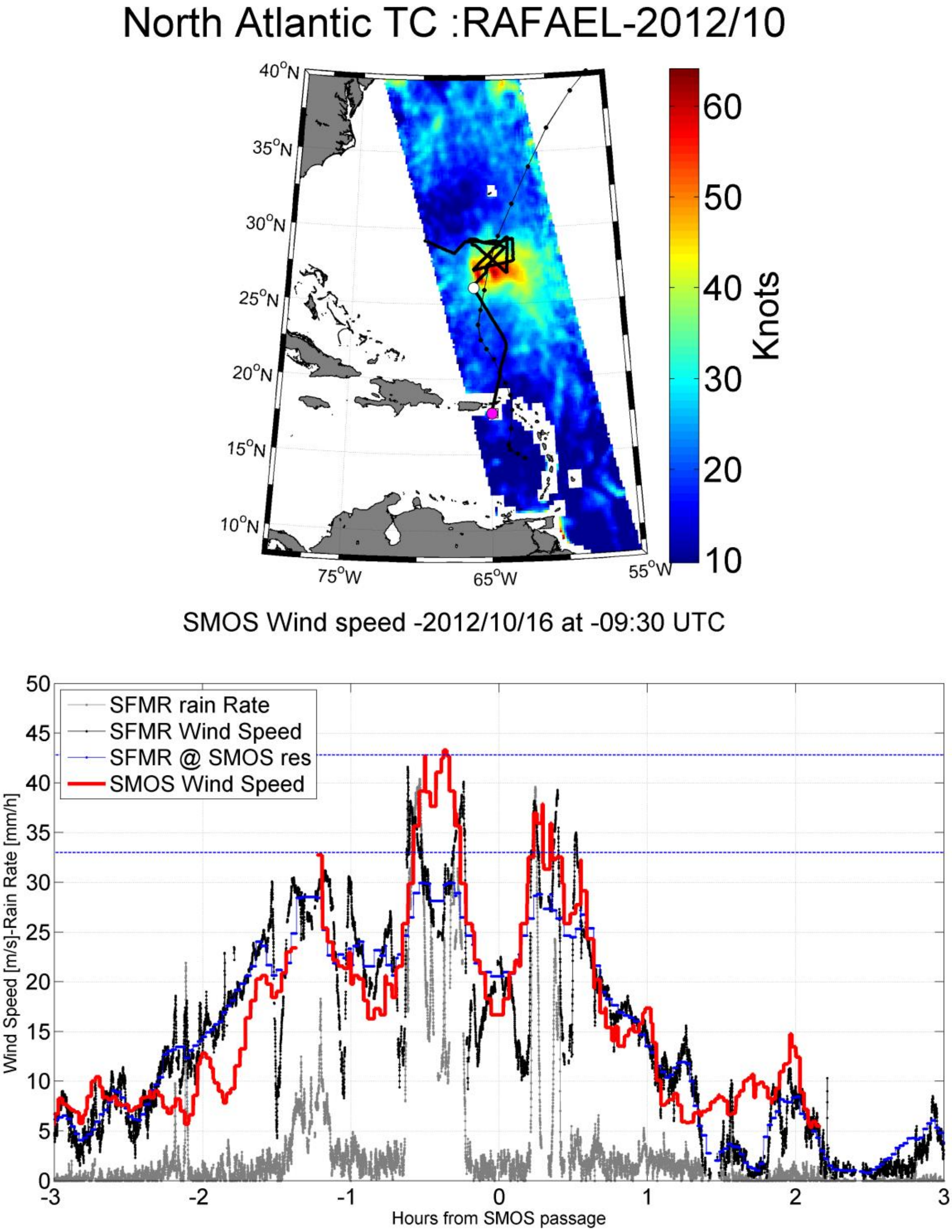

Figure 12: Idem than Figure 10 but for Hurricane Rafael on 16 November 2012.

To minimize the potential impact of the storm structural evolutions in between SMOS and SFMR acquisition times, we selected only those match-ups with $|\Delta t| < 0.5$ h. The storm-induced excess L-band emissivity as function of the co-localized SFMR wind speed spatially smoothed at SMOS resolution and obeying the previous time lag constraint is shown in Figure 13. The median and standard deviation of the Δe values per 5m/s-width bins of SFMR wind speed are also provided. For comparison, we show the Reul et al., 2012 bi-linear GMF.

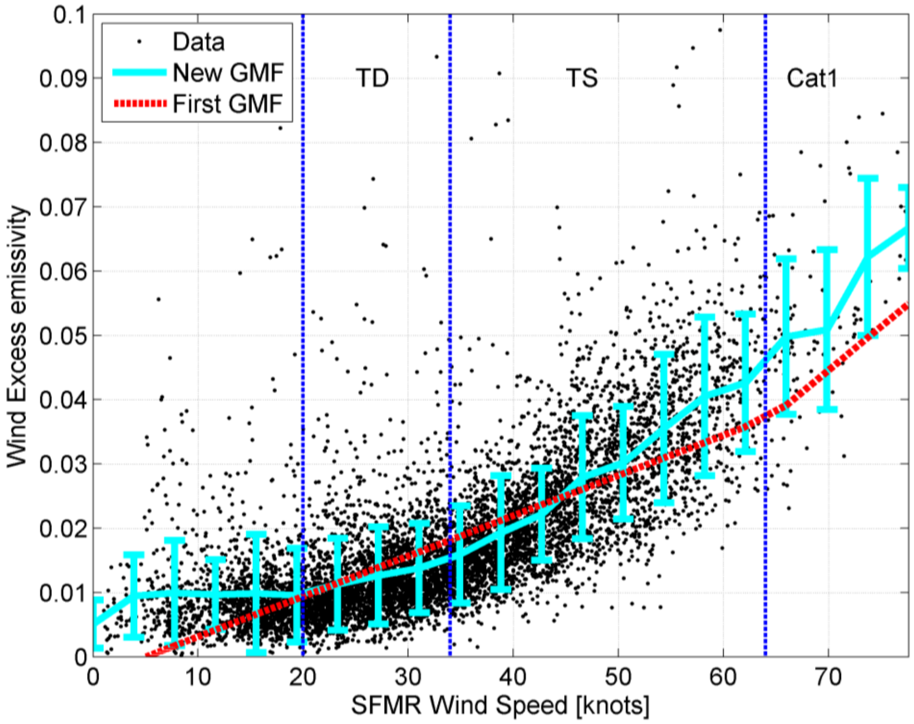

Figure 13: SMOS storm-induced excess L-band emissivity as function of co-localized SFMR wind speed collected for an ensemble of 64 flights. The time lags between both observations never exceed 0.5 h. The red line indicate the first bi-linear GMF proposed in Reul et al., 2012. The cyan curve indicate the mean wind-excess emissivity per 5 m/s-width bins and the vertical bars indicate ±1 standard deviation of the emissivity within each bin.

As can be seen, while rather close to the first bi-linear GMF estimate, the new GMF based on SMOS-SFMR wind speed match-ups is a nonlinear function of the wind speed. In particular, the new GMF shows that the storm-induced excess emissivity is almost wind-speed independent for winds below 20 knts (~10 m/s) and equal to ~0.01. In the intermediate wind speeds ranging from 20 to 45 knts (23 m/s) the linear GMF lies above the new non-linear relationship indicating a potential underestimation of the retrieved wind speed from SMOS data using the linear empirical law. In the highest wind speed regime (>45 knts), the reverse is observed with the new GMF function showing systematically higher values than the linear one.

5.2 Systematic comparisons between SMOS and H*WIND

The SMOS-SFMR co-localized datasets evidenced that the first GMF's linear empirical law allows in general to retrieve relatively accurate surface wind speed values from SMOS observations in TCs. However, it also highlights a slightly more non-linear behaviour of the Δe as function of surface wind speed than the one we found from IGOR case-only, particularly in the intermediate (10 to 20 m/s) and high (20-40 m/s) wind speed ranges in which the use of the bilinear GMF function might result in under and over estimation of the surface wind speed, respectively. Given the time-lag constraints in the SMOS-SFRM data co-localization and data selection involved in building the GMF, a small amount of match-ups were nevertheless available in the highest wind speed regime with very little data above hurricane force (>64 knts~32 m/s). To increase our confidence in the statistical reliability of the GMF and to gain in quantity of match-ups at the highest winds, we therefore conducted an ensemble of additional co-localizations between SMOS Δe, retrieved SWS (using first GMF as a guess) and H*WIND 2D SWS fields. We found about 30 cases for which either SMOS intercepts data were available within less than 0.5 hour from an H*WIND or with the two closest H*WIND wind fields in time (before and after a SMOS overpass of storms) available within 12 hours. In the latter case, an interpolation in time of the two closest storm-centric H*WIND SWS fields was performed at the SMOS time.

For illustration, we provide in Figures 14 and 15 two examples of SMOS/H*WIND comparisons. Figure 14 shows the results for Hurricane Leslie as it developed to become a Tropical Storm the 7 Sep 2012 at 22:19 Z. The rms difference between SMOS and H*WIND SWS fields is ~4m/s. As seen, the structure of both wind fields are very consistent in general, with maximum winds found in the North-West quadrant at a radial distance of about 150 kms and the radii at 34 and 50 knts matching closely between both products in the North West and South east quadrants. Nevertheless, small residual biases are seen in the two other quadrants, with SMOS winds lower than the H*WIND ones and with a smaller 34knts radius in the southwest quadrant.

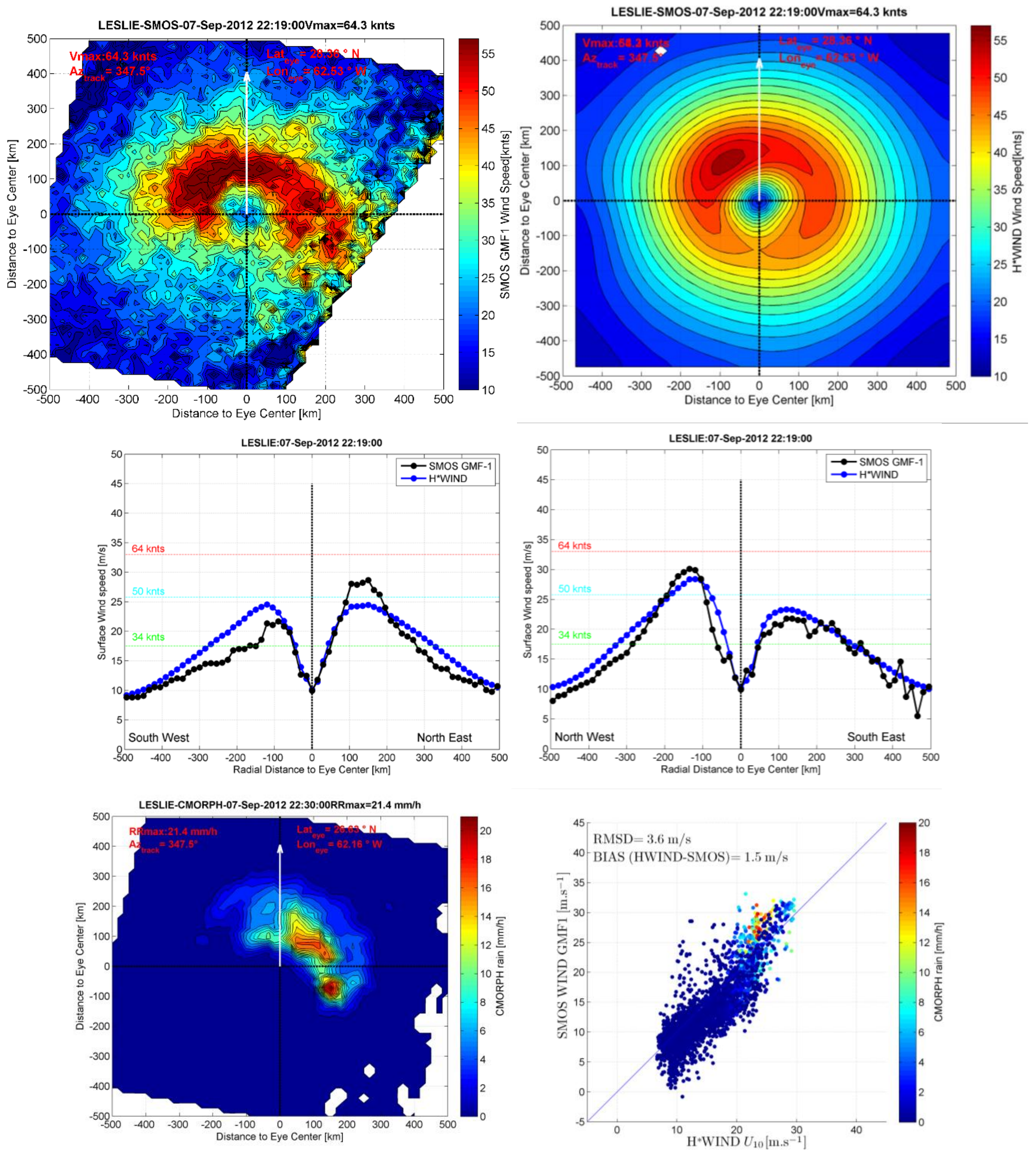

Figure 14 : Top left: Surface wind speed retrieved from SMOS (first GMF) in a storm centric coordinate system as the instrument intercepted hurricane Leslie the 7 sep 2012 at 22:19. Top right: H*WIND fields interpolated at SMOS acquistion time and spatially averaged at 43 km resolution. Middle panels: Mean radial distribution of the SMOS (black) and H*WIND (blue) SWS from the South West to the North East storm quadrants (left), and from the North West to the South East storm quadrants (right). Bottom left: CMORPH rain rate at SMOS acquisition time. Bottom right: SMOS retrieved wind speed as function of H*WIND with color indicating the rain rate from CMORPH.

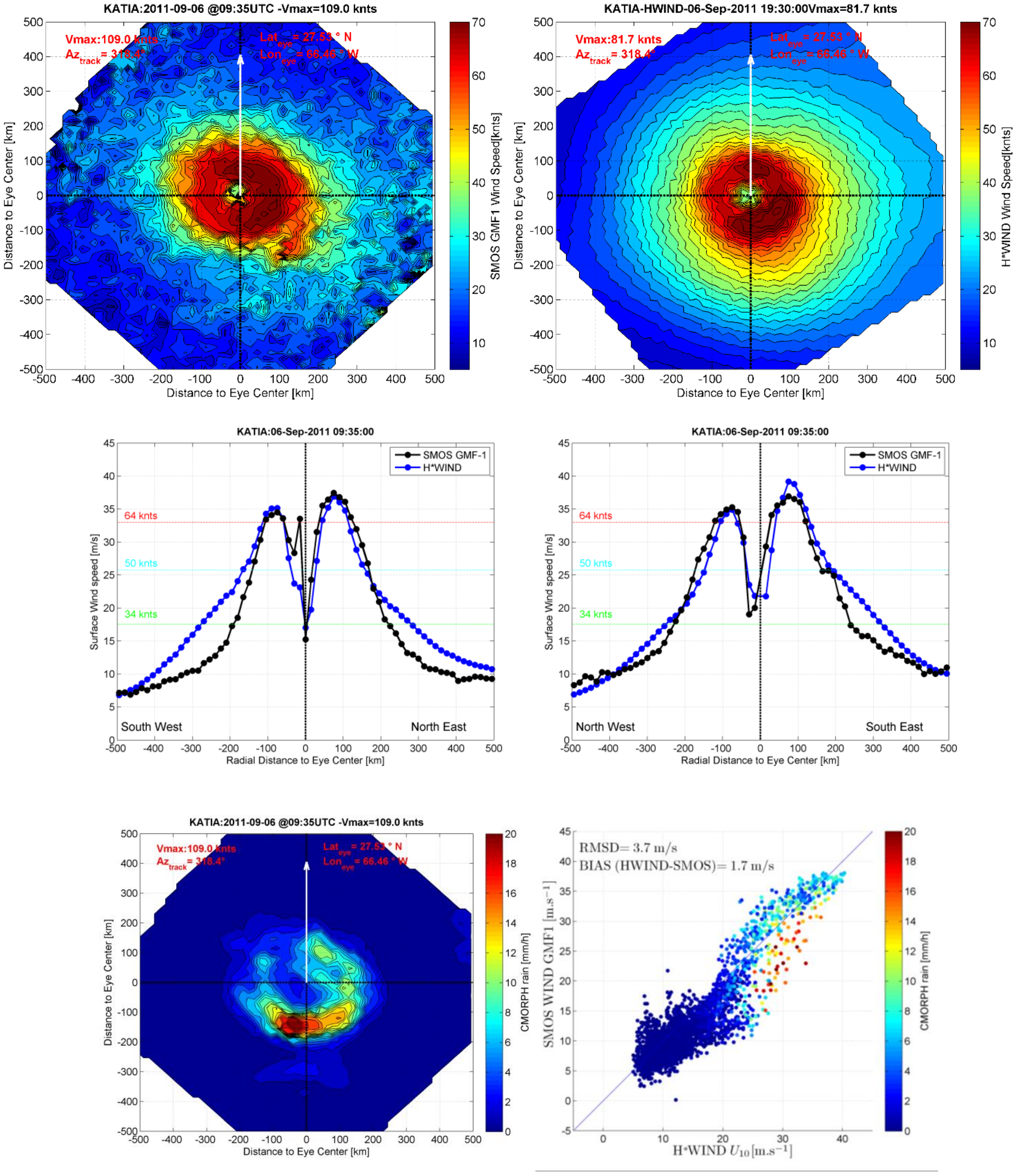

Figure 15: same legend than in Figure 16 but for the case of Hurricane Katia the 6 September 2011 at 09:35 Z.

SMOS winds are slightly higher than H*WIND in the North East quadrant. As revealed by CMORPH data, rain rate was important reaching more than 20 mm/h at some locations in the highest wind speed band of this quadrant and the higher the retrieved SMOS winds there with respect H*WIND, the highest were the rain rates (see Figure 14, bottom panels).

The second example shows the case of Hurricane Katia as it reached a Category 2 intensity. Here again, the match between both SMOS and H*WIND wind speed fields is rather good in general (rmsd~3.7 m/s), showing consistent estimates of the maximum wind radius and value around 80 knts, and of the 50 and 64 knts wind radii. Here again, SMOS retrieved winds around 34 knts are nevertheless exhibiting a slightly smaller wind radii than the H*WIND product. This is consistent with the behaviour expected from the bilinear GMF according to SMOS/SFMR matchups. However, and contrarily to the case of Leslie, the intense rain region (with rain rates >20 mm/h) is here associated with underestimated winds from SMOS with respect H*WIND while it was associated with overestimated winds in the previous example of Leslie, suggesting that rain is not the principal process responsible for the observed biases in SMOS versus H*WIND (see Figure 15, bottom right panel).

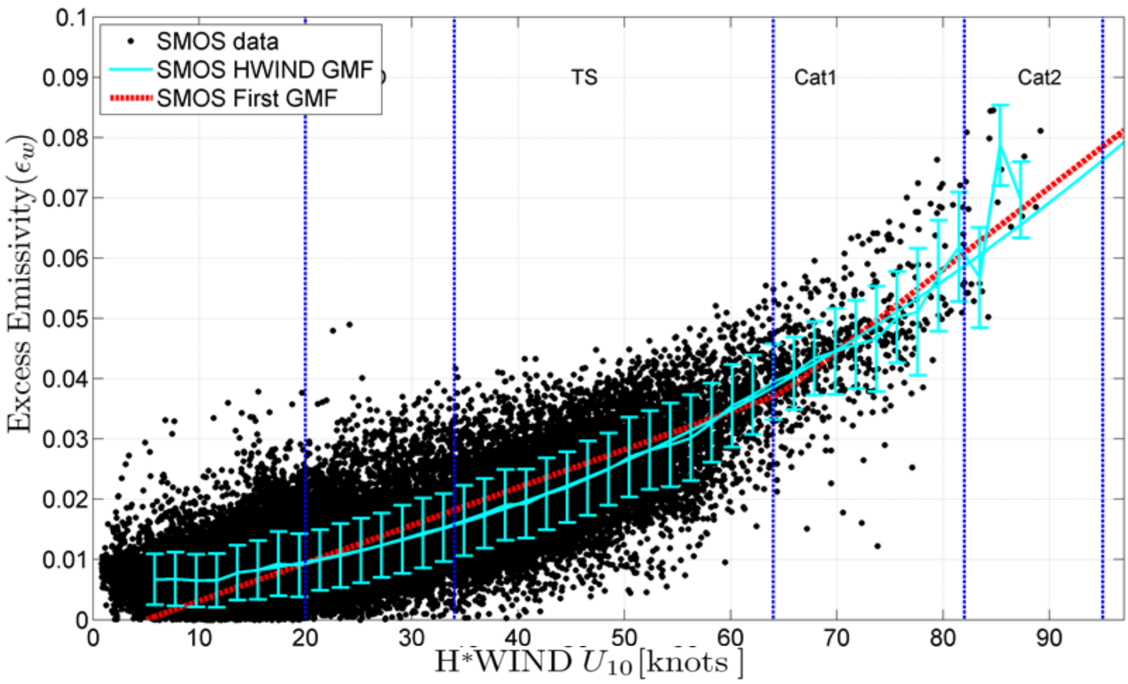

Figure 16: Wind Excess emissivity as function of co-localized HWIND wind speed collected for an ensemble of storms in between 2010 and 2013. The red curve illustrates the SMOS first GMF. The cyan curve show the new 'average' GMF function based on the SMOS/HWIND match-ups. The excess emissivity data were averaged per 5 knots bins of HWIND winds with vertical bar indicating ± 1 standard deviation of the Δe within each wind speed bin.

By cumulating the 30 2D fields co-localized between SMOS radio-brightness contrasts and H*WIND, we re-analyzed the GMF with a more consequent ‘ground-truth’ dataset. This is illustrated in Figure 16, which shows the storm-induced excess emissivity as function of H*WINDs 1 mn sustained winds spatially averaged at 43 km.

Below 50 knts, the deduced GMF is showing in general very similar differences with the bi-linear one than the previous GMF deduced using only SFMR data (this is somehow expected as SFMR data are used as key input data to derive the H*WIND analyses): the newly derived GMF from SMOS/HWIND is non-linearly, almost quadratically, dependent on wind speed with lower Δe values than the linear law between 20 and 50 knts. In the wind speed regime over 50 knts, the H*WIND derived GMF is well reproducing the first GMF which was not the case for the SFMR matchups. A quadratic fit through the data give the following GMF function for the half-power L-band storm-induced brightness temperature contrast as function of the H*WIND 1mn sustained surface wind speed averaged at SMOS spatial resolution:

$$\Delta I(U_{10}) = SST \cdot (2.7935 \times 10^{-5} U_{10}^2 + 6.8599 \times 10^{-5} U_{10} + 0.0059) \qquad \text{Eq (1)}$$

As H*WIND and SFMR–based fits are very similar in the low to moderate wind speed range and given the fact that the H*WIND GMF is based on SFMR data but also that this dataset provide a much higher number of match-ups at high wind, in the following we will use the H*WIND-based expression of the GMF (Eq.1) as the new reference GMF for retrieving surface winds from L-band radio-brightness contrasts data.

5.3 Potential Impact of Rain

The previous GMFs were built assuming that there is no impact of rain and sea state on the L-band contrasts. Using CMORPH co-localized 2D observations, all data used to build up the H*WIND-based GMF can be now characterized in terms of rain rate. In figure 17 top panel, we show the bin-averaged Δe as function of wind speed for rain free and rainy conditions. Data showing both conditions are only available up to 50 knots. The figure evidences that in this range of surface winds, the rain free emissivity contrast at a given wind speed is systematically lower than the equivalent one measured in rainy-conditions. The differences in emissivity contrasts between rainy and non-rainy conditions reach a maximum of ~0.01 observed at 50 knts, which at an SST of 28°C would translate into a 3 K shift in ΔI due to rain.

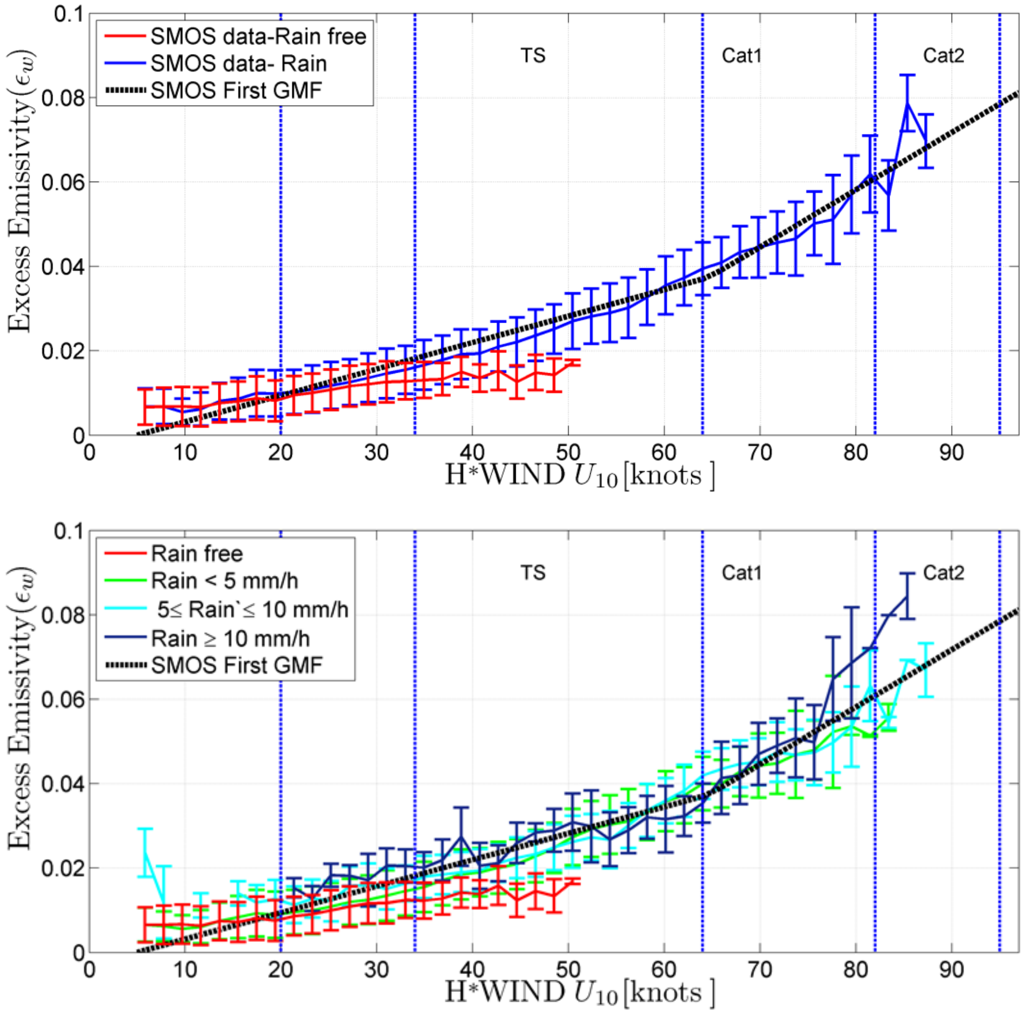

Figure 17: Potential effects of rain on the excess L-band emissivity in storm conditions. Top: GMF deduced from the SMOS-HWIND matchups with rain rate provided from CMORPH=0 (red) and rain rate > 0 (blue). Bottom: idem except that the data are now classified by ranges of rain rate (RR): RR=0 (red), 0<RR≤5 mm/h (green), 5mm/h<RR<≤10 mm/h (cyan) and RR>10 mm/h. (blue).

According to the sensitivity of the GMF (~0.3 K/ m/s below hurricane force and ~0.7 K/(m/s) above 32 m/s=64 knts), the rain effect might therefore translates into maximum wind speed retrieval errors of 10 and 5 m/s below and above hurricane force, respectively. In figure 17 bottom panel, we show the data further classified as function of rain rate intensity. No clear stratification of the Δe as function of increasing rain rate is observed in the data, with all observations in rainy conditions lying close around the bi-linear GMF. This can potentially indicates that the rain is not directly responsible for the difference of emissivity between the rain-free and rainy conditions. Small ice particles are known to exist between the eyewall and outer rainbands, of TCs and graupel particles are often collocated with the radius of maximum tangential wind (Houze et al., 1992). Hurricanes are usually glaciated everywhere above the −5°C level and the stratiform areas are dominated by snowflakes (aggregates) at these levels (Black and Hallett., 1986). The variation of ice phase cloud characteristics on the top of the cyclones and the associated varying contributions of these clouds to the L-band emission between the rainy and rain-free conditions might be a plausible source for the observed differences in Δe. Nevertheless, no data characterizing the upper atmosphere in terms of ice-phase content is available to estimate that effect.

5.4 Validation of SMOS winds and relative accuracy with ECMWF and NCEP

The SMOS GMF given in Equation 1 was derived based on an ensemble of 30 H*WIND products, covering about 20 storms in the Atlantic and Gulf of Mexico over several years. The first bi-linear GMF from Reul et al., 2012 was only derived based on 2-3 H*WIND fields during Hurricane Igor in 2010. Validating the new GMF with the H*WIND data as a limited interest as the latter were already used to derive the GMF per construction. To assess the performance of SMOS winds with respect NWP products using the 30 collected H*WIND fields as the validation dataset, we therefore use the wind speed retrieved based on the first GMF. ECMWF and NCEP surface winds were co-localized with the storms intercepted in the 30 pairs of SMOS-HWIND data fields.

There might be some residual rain or ice effects degrading the quality of the retrievals as discussed in the previous section. However, given the fact that we don’t have yet a methodology to correct for these effects, they are neglected in the comparisons that follows. The differences between H*WIND and the SMOS SWS were evaluated using the bilinear GMF function that was quasi-independently derived from the H*WIND dataset used for here validation. In Reul et al., (2012) we estimated based on IGOR case alone that the rms error on wind speed was on the order of 5 m/s. This new validation against the 30 H*WIND 2D fields shall provide a more reliable quality assessment of the relative quality of SMOS wind speed products as based on a significantly larger ensemble of match-ups. SMOS, ECMWF and NCEP surface winds are compared to the reference H*WIND fields in Figure 18.

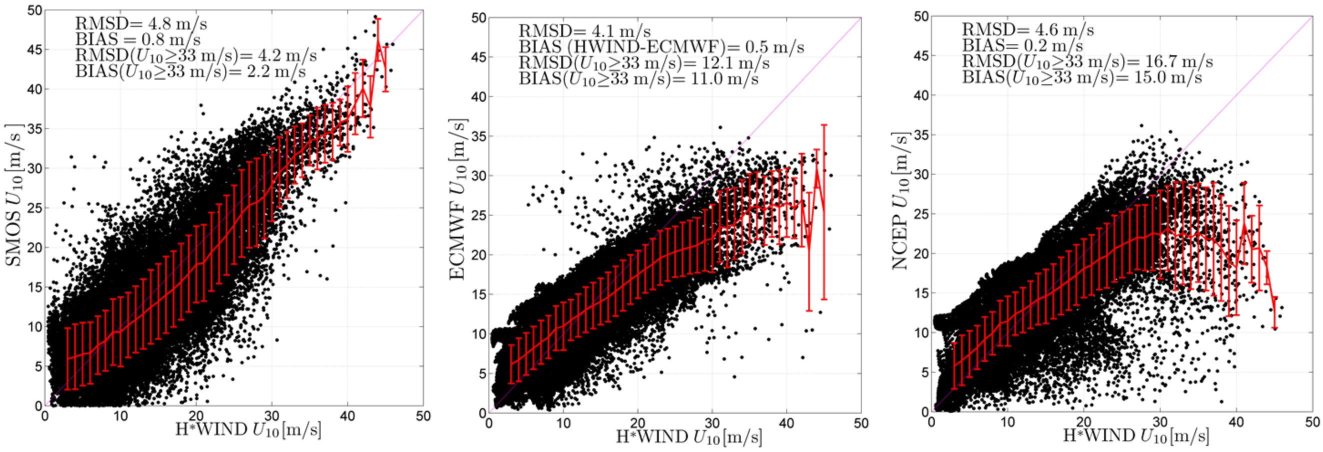

Figure 18: Comparisons between co-localized SMOS, ECMWF or NCEP wind speeds and HWIND ones for an ensemble of ~30 intercepts with tropical storms and hurricanes over the period 2010-2013. Left: SMOS retrievals (first GMF) versus H*WIND, ECMWF winds (Middle) and NCEP (right) winds versus HWIND. The red curves are showing the mean y-axis wind speed in bins of 1 m/s width of HWIND SWS data ±1 standard deviation. Root mean square differences (RMSD) and biases between each products and Hwind ones are provided in each panel for the complete wind speed range and for the hurricane wind speeds (>33 m/s).

Statistics of the differences between these three estimates of the surface wind speed in TCs and H*WIND data are provided in Table 1.

Table 1: Statistics of the differences between co-localized H*WIND and SMOS, ECMWF and NCEP surface wind fields (positive mean difference means that H*WIND is greater than the considered product).

	Wind Speed Range (m/s)	**SMOS**	**ECMF**	**NCEP**
RMSD (m/s)	0-50	4.8	4.1	4.6
Mean difference (m/s)	0-50	0.8	0.5	0.2
RMSD (m/s)	33-50	4.2	12.1	16.7
Mean difference (m/s)	33-50	2.2	11.1	15

As shown in table 1, the rms and mean differences between H*WIND products and the three surface wind speed products are very similar considering the full wind speed range between 0 and 50 m/s, ranging from 4 to 5 m/s, and 0.2-0.8 m/s, respectively. At hurricane force above 33 m/s, SMOS wind speed accuracy nevertheless outperforms the NWP winds with rms and mean differences between SMOS and H*WIND data of about 4 m/s and a 2 m/s, respectively; both NCEP and ECMWF products hardly reach wind speed values above hurricane force as both saturate with increasing wind speed to show rms differences and biases with H*WIND significantly above 10 m/s in this high wind speed range.

We clearly showed in the previous section that the ‘average’ temperature excess is a monotonically increasing parameter with increasing the storm intensity. An important question is to investigate whether the maximum sustained wind speed, a key parameter in all parameterization of hurricane wind field dynamics, can be retrieved from SMOS given the relatively low spatial resolution of the instrument. The highest winds regions are often extending over domains with typical scales on the order of, or smaller than, 100 km, with very significant wind speed gradients found over small distances relative to the SMOS pixel size, particularly in the eyewall region. This results into spatial smoothing of the maximum wind values: the stronger the gradients over short distances, the more important the attenuation effect: this was clearly observed when comparing SMOS retrievals with SFMR high and low resolution observations.

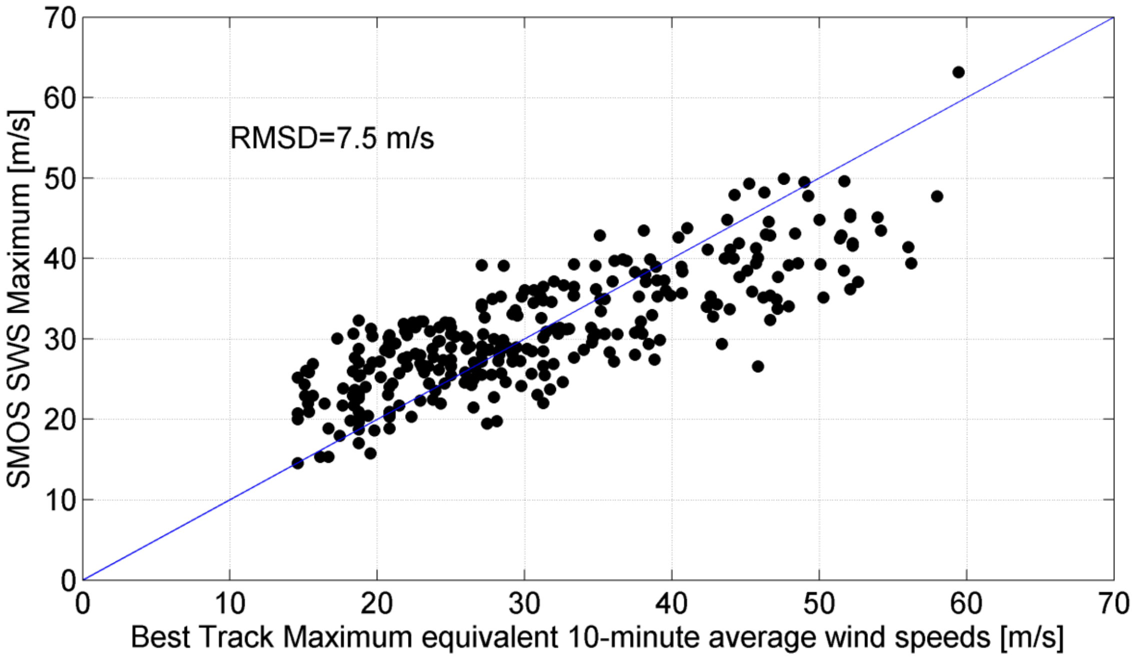

Figure 19: Relationships between the maximum of SMOS winds as function of the Best track Maximum Sustained Wind speed.

To assess the quality of the maximum wind speed inferred from SMOS products, we compared the maximum wind derived from the second GMF in each of the 300 intercepts selected from the SMOS-STORM database to the maximum wind interpolated at SMOS time from the 6-hourly best track data. The comparison between both estimates shown in Figure 19 reveals that the maximum wind derived from SMOS in general correlates well with the Best-track maximum sustained wind. The rms difference is nevertheless higher than it was found for the all-wind speed comparisons, reaching ~ 7.5 m/s. An underestimation of the maximum wind is also systematically visible in the SMOS products, the higher the wind speed above ~40 m/s. Sources for this limitation is likely the previously discussed spatial-smoothing effect of the satellite sampling, with a predominant impact in the very high wind and high gradient regions.

6 Conclusions and perspectives

Five years (May 2010- April 2015) of SMOS L-band brightness temperate data intercepting a large number of Tropical Cyclones at global scale have been analysed in this paper. A subset of about 300 intercepts were carefully selected to provide the highest quality observations available covering the full range of storm intensities on the Saffir-Simpson High Wind Scale (SSHWS). The storm-induced half-power radio-brightness contrasts ΔI were estimated for each SMOS intercept of the storms and expressed in a common storm-centric coordinate system.

The 2D mean and standard deviation of the ΔI were further evaluated for each intensity classes of the SSHWS. The averaged distributions of ΔI show that the mean brightness contrast amplitude is coherently increasing with the increasing intensity of TCs. The radii within which the brightest ΔI values are found for each category is also seen to diminish as the storm intensity increases, consistent with the reported evolution of the highest surface wind distribution in TCs (Holland, 1980). A remarkable feature of the mean ΔI fields is that the maxima of ΔI are systematically found on the right-hand sides quadrants of the storms. Here again, this is consistent with the reported asymmetric structure of the wind and wave fields in hurricane, with the maximum in wind speed and sea surface heights generally occurring in the right-hand side quadrants of the storms (in the northern-hemisphere) because of the relative wind and extend-fetch effects created by a translating storm. For categories 1-5 TCs, the brightness standard-devation is showing a quasi-annular distribution around the storm centers, with local minima at the center, a signature of the relatively calm eye of the TCs and local maxima in the right-hand quadrant of the storms. For storm intensities above and including category 4 on the SSHWS, the instrument however hardly resolves the detailed TC eye structures for those most intense storms which exhibit maximum wind radii below the SMOS pixel size (~43 km). The mean brightness contrast is monotonically increasing with storm intensities from about 5K for tropical storms up to ~22K for the most intense category 5 cyclones without showing saturation above hurricane force (32 m/s) illustrating the potential of the SMOS data for better monitoring TC intensification.

A bi-linear GMF relationship between ∆I and the 10 m height surface wind speed U_{10} has been first proposed in Reul et al., 2012. This first GMF was inferred solely from very few observations acquired over a single north-Atlantic hurricane event (Category 4 hurricane IGOR in 2010). A revision of that GMF has been provided in this paper using a much larger ensemble of co-localized SMOS, SMFR flight track data and analysed 2D H*Wind fields. In average, we found that the L-band radio-brightness contrast evolves quadratically with surface wind speed and we proposed an empirical parametric law relating ∆I and the 10 m height surface wind speed U_{10} . Major differences with the first bi-linear GMF of Reul et al., 2012 are found in the low to moderate wind speed regimes. Use of the new GMF shall help reducing observed biases in the SMOS surface wind retrievals below 50 knts.

Using co-localized rain rate estimates from CMORPH, we have shown that the L-band radio-brightness contrast measured in TCs in rain-free conditions do not evolve similarly with wind speed than the one acquired in rainy ones. Differences can reach up to 3K, which might translate into maximum SWS retrieved errors of ~10 m/s below hurricane force (~32 m/s) and 5 m/s above. Larger errors are found in the lowest wind speed regime because of the smaller sensitivity of the ∆I function to wind speed below hurricane force. Further classifying the data as function of increasing rain rate for fixed wind speed values, we couldn't however evidence any clear dependencies with increasing rain rate. This seems to indicate that other geophysical contributions might explain the observed differences in ∆I between rain-free and rainy conditions: the variation of ice phase cloud characteristics on the top of the cyclones and the associated varying contributions of these clouds to the L-band emission might be a plausible source.

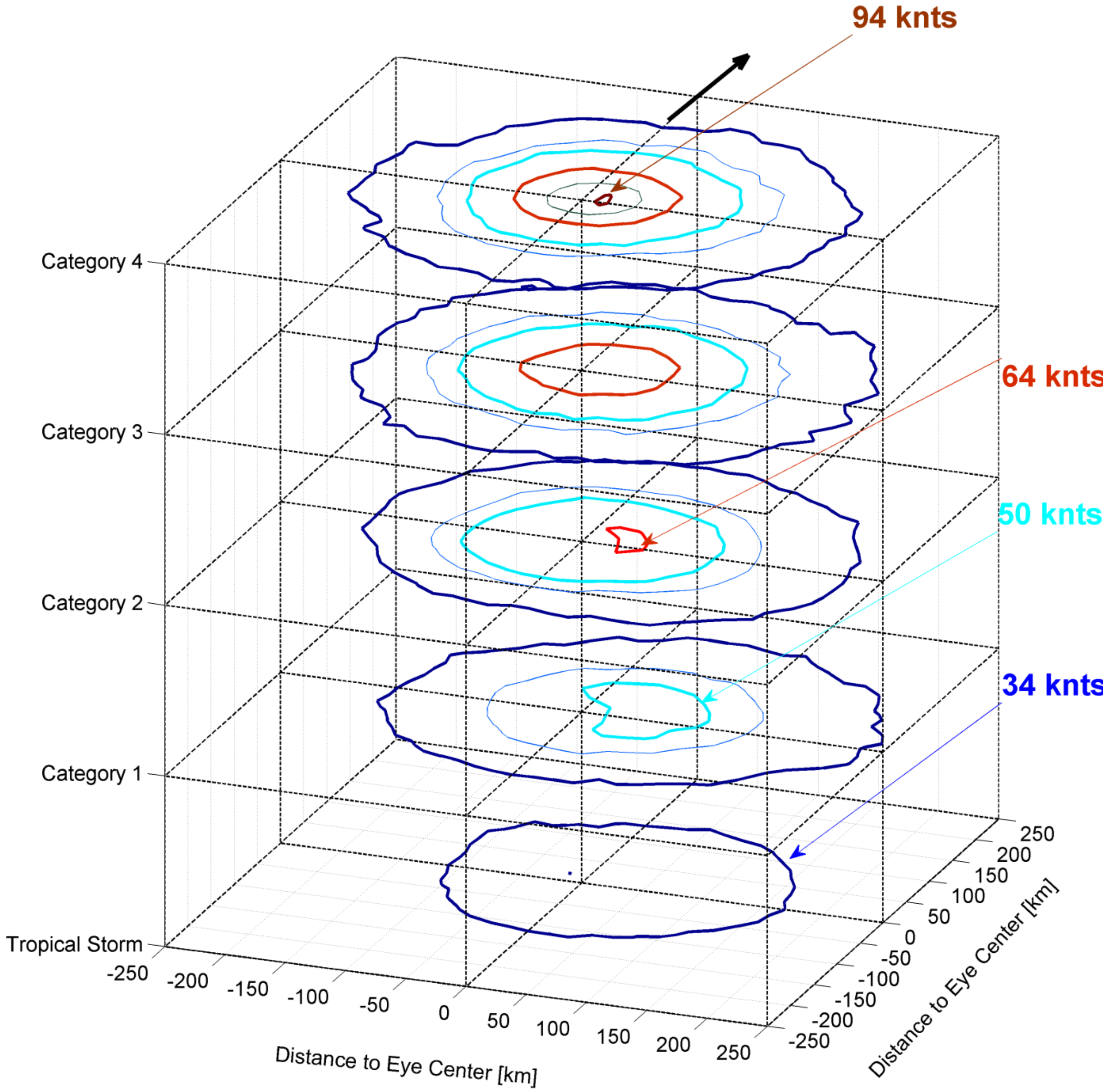

Figure 20: Synoptic structure of the surface wind field in Tropical Cyclones as retrieved from SMOS data as function of the Saffir-Simpson High Wind intensity scale. Average 2D wind fields from SMOS are contoured at levels of 34 (thick dark blue), 44 (thin blue), 50 (thick cyan), 64 (thick red), 80 (gray) and 94 (thick chesnut) knts. The thick black arrow is indicating the averaged storm propagation direction.

Neglecting the potential rain/ice impacts, we compared SMOS, ECMF and NCEP winds to a large ensemble of H*WIND 2D fields spatially averaged at the SMOS ~43 km nominal spatial resolution. Results showed that the surface wind speed in TCs can be retrieved from SMOS data with an rms error on the order of 4-5 m/s up to 50 m/s. The SMOS wind product performances when compared to H*WIND ‘ground-truth” data in the hurricane wind speed range (above 32 m/s) are a factor 3 to 4 better than the one from the NWP products, which are heavily underestimating the surface wind speed in these extreme conditions. The maximum wind speed estimated from SMOS was shown to be consistent with best-track estimates but also exhibits a degraded rms error of ~7.5 m/s compared to the all-wind results. This degraded accuracy for the maxima is thought to be induced by 1) the spatial-smoothing effect of the instrument sampling in the high-wind gradient zones of the eyewalls and 2) a potentially higher effect of rain and cloud ice on the L-band emissivity in these regions.

Applying the new quadratic GMF function to the average radio-brightness contrasts estimated as function of storm intensities, we are now in a position to provide a synoptic view of the surface wind field observed by an L-band passive sensor in tropical cyclones and its structural evolution as function of increasing TC intensities. This is illustrated in Figure 20 where is shown the average structure of the surface wind field in Tropical Cyclones as retrieved from SMOS data as function of the Saffir-Simpson High Wind intensity scale. Average 2D wind fields from SMOS show that the radii of the most intense winds always start to appear on the RHS quadrants of the storms for a given intensity. As the storm intensity increases, the wind speed above a certain threshold spreads within a quasi-circular domain of almost constant radii: ~200 km for winds above 34 knts, 120 km for winds above 50 knts and ~75 km for winds above 64 kts. Following the approach of Chavas and Emanuel, (2015) who used an historical datasets of QuickSCAT observations to analyse the wind structures in the outer region of tropical cyclones at large radii, the SMOS synoptic wind structure could be used to assess the quality of available Hurricane wind models (e.g. Holland, 1980) for almost the complete radial structure of the low-level tropical cyclone wind field. This task is left for future work.

An important result of this study is that the average L-band brightness temperature systematically indicates maxima in the RHS quadrant of the storms above hurricane force.

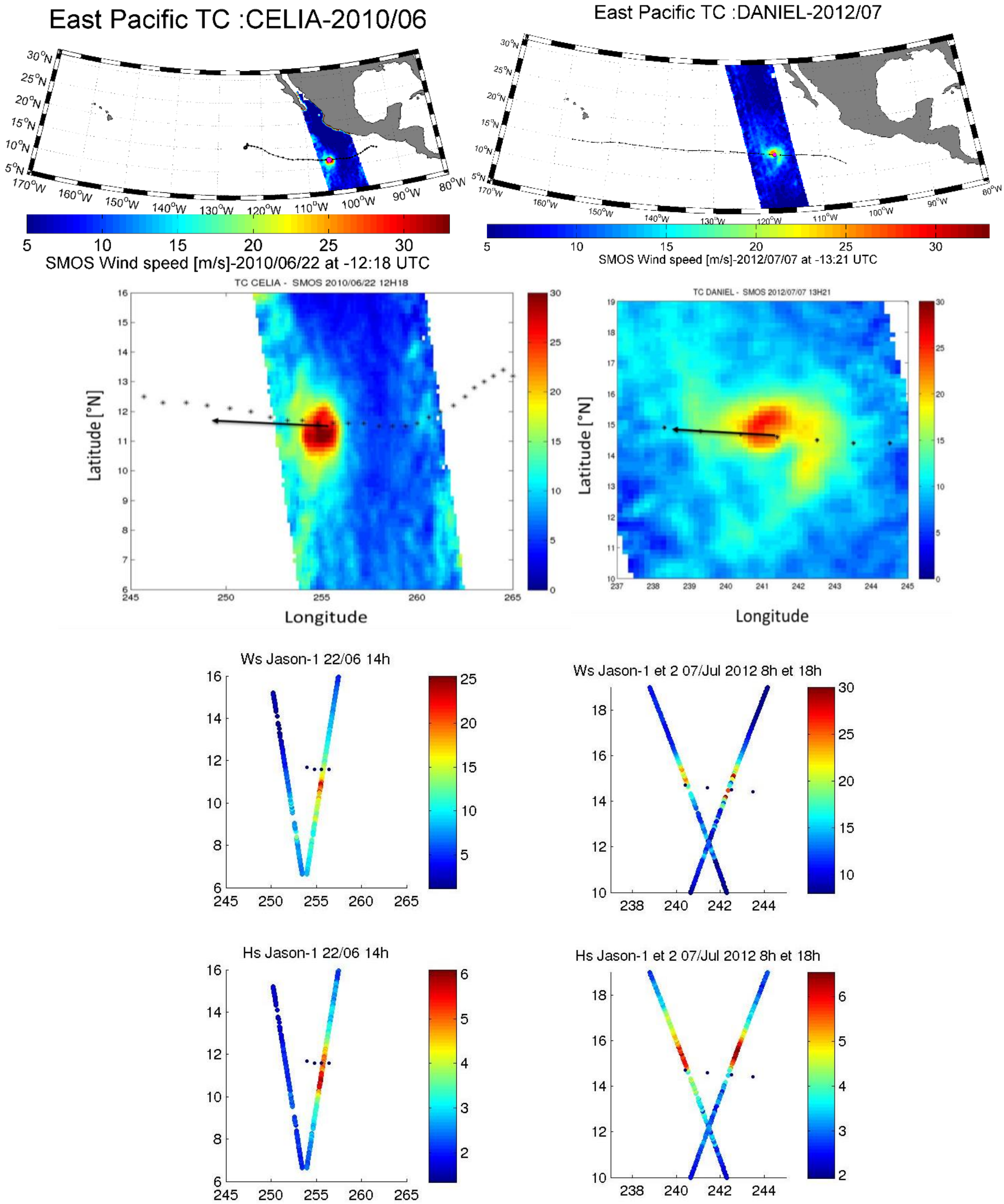

Figure 21: Top: large-scale views of SMOS swath retrieved wind speed as the instrument intercepted 2 TCs propagating westward in the eastern pacific: Celia the 22 june 2010 at 12:18 UTC (left) and Daniel the 7 july 2012 at 13:21 UTC. Middle: blow-up on the corresponding retrieved SMOS wind fields. The asterixes and the arrows indicate the eye-tracks and their translation directions, respectively. Third panels show the surface wind speed estimated along Jason-1 track at 14h as it intercepted Celia (left) and the one from Jason-1 (8h) and 2 (18h) as they intercepted Danielle. Bottom panels show the significant wave heights evaluated along each altimeter tracks.

This is consistent with reported structures in TC wind models but waves and associated generation of foam are also known to show large asymmetries in storm quadrants with clearly evidenced maxima in significant wave height found in the RHS quadrants because of the ‘extended-fetch’ effect (Young, 2003). The relative contributions of wind and waves to the increase of L-band radio-brightness contrasts remain uncertain and need detailed investigation, using, e.g., systematic co-localizations between SMOS data, ground-truth surface winds, and wind & sea state measurements from altimeters (Quilfen et al., 2011). This is an on-going research that our team conduct in the frame of the ESA STSE SMOS-STORM project that funded the present study. Two interesting preliminary examples of consistent quadrants asymmetries revealed in both SMOS and altimeter data are shown in Figure 21. Hurricane Celia (2010) and Daniel (2012) both developed in the eastern Pacific (northern-hemisphere) as their eye translated towards the west. According to the wind and wave development theories in TCs, maximum wave height and winds shall be found on the RHS of the tracks. As illustrated in Figure 21, middle panels, this was clearly the case for hurricane Daniel but not for Celia, for which the SMOS retrieved winds clearly exhibit a maximum on the LHS of the storm track. These observed quadrant asymmetries are very consistent with the altimeter observations of both retrieved wind and wave height, although the altimeter-derived SWS in Daniel is affected by rain: Jason-1 clearly show maxima in wind and waves on the LHS and RHS quadrants of Celia, and Daniel, respectively. A large ensemble of such SMOS-altimeter co-localized data shall help us in the future inferring the statistical impact of waves and sea state relative to the wind effect.

A very promising perspective is the creation of a passive low-microwave frequency-based SWS products storm catalogue that would be built by merging SWS data in TCs inferred from SMOS, AMSR2 and SMAP sensors. An illustration of such enhanced storm tracking capability by merging SMOS and AMSR2 is given in Figures 22 and 23 for the case of the super typhoon Haiyan that devastated Philippines in Nov 2013. Typhoon Haiyan (known in the Philippines as Typhoon Yolanda) slammed into the Philippines in November 2013 with sustained winds of 310 kilometers per hour, making it one of the strongest tropical storms to date and the second-deadliest Philippine typhoon on record. Haiyan originated from an area of low pressure in the Federated States of Micronesia on November 2 (see Figure 22 top panel).

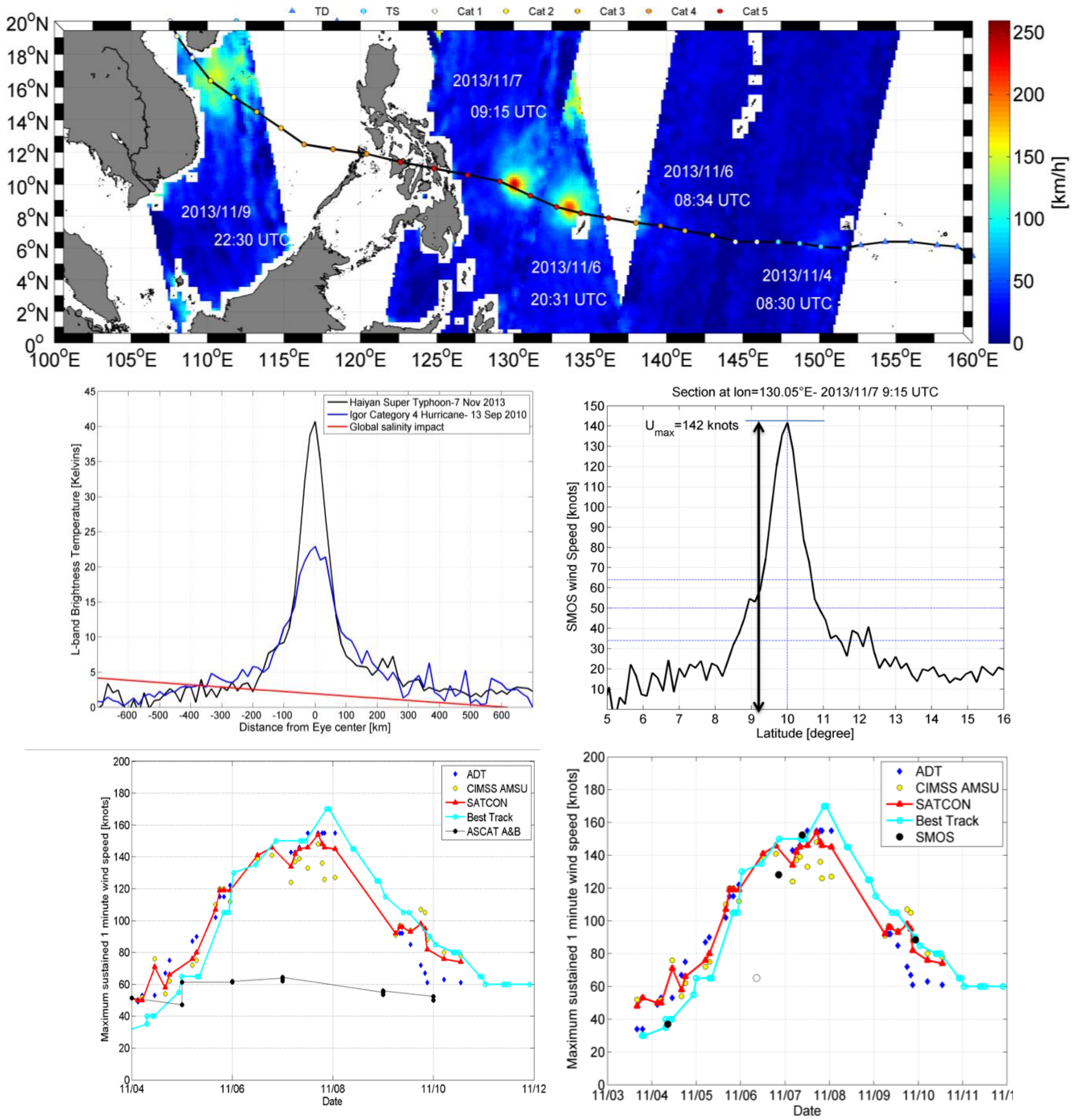

Figure 22: Ensemble of SWS fields retrieved from the SMOS swaths that intercepted super typhoon Haiyan in November 2013. Middle left: L-band radio brightness contrast ΔI measured along a South-North section passing through the eye of super Typhoon Hayian (black) as it reached category 5 intensity on 7 November 2013 and Category 4 hurricane Igor the 13 Sep 2010. The range of variations of ΔI for all possible SSS and SST values is given by the red line. Middle right: SMOS retrieved wind speed [knts] along the South-North section through Haiyan. Bottom left: Maximum sustained 1 minute wind speed estimated during Haiyan Typhoon. From ASCAT A &B data (black filled dots) compared to estimates made available by the Cooperative Institute for Meteorological Satellite Studies (CIMSS, see http://tropic.ssec.wisc.edu/): Advanced Dvorak Technique (ADT=blue diamond), CIMSS (yellow filled dots), SATCON (red) and Best Track from NHC (cyan).. Bottom right: idem than the left panel but with the maximum wind speed from SMOS (black filled dots). Note the empty circle corresponds to the SMOS measurements for the 6 November (am) for which only a small portion of the cyclone signal was intercepted. 10 minutes wind speed deduced from SMOS algorithm were multiplied by 1/0.93, adopting the conversion factor proposed in (Harper et al., 2010) between one minute winds and 10 min winds.

Tracking generally westward, environmental conditions favored tropical cyclogenesis and the system developed into a tropical depression the following day. After becoming a tropical storm and attaining the name Haiyan at 0000 UTC on November 4, the system began a period of rapid intensification that brought it to typhoon intensity by 1800 UTC on November 5. By November 6, the Joint Typhoon Warning Center (JTWC) assessed the system as a Category 5-equivalent super typhoon on the Saffir-Simpson hurricane wind scale; the storm passed over the Palau shortly after attaining this strength.

SMOS intercepted the typhoon several times along its track. We selected only those passes were the signal was well detected and not too contaminated by RFI or land masses. As illustrated by Figure 22, this let one pass on the 4 as Haiyan was still a Tropical Storm, two on the 6th Nov (with the morning pass capturing only a small portion of the typhoon), one on the 7 prior landing towards Philippines and one interception on the 9, just before it passed over Vietnam. Passes on the evening of the 6 and during the 7th morning were close in time from the maximum intensity reached by that super storm (reached on the evening of the 7th). As illustrated by Figure 22 middle left panel, the estimated excess brightness signal (First stokes parameter/2) due to surface roughness and foam-formation processes under the cyclone on the 7th morning overpass (i.e., after correcting for atmosphere, extra-terrestrial sources, salinity and temperature contributions) reached a record value of 41 K. To put such value in perspective of other natural oceanic signals, we plotted together the Tb jump measured during the passage of Hurricane Category 4-5 Igor in 2010, which was only 22 K! In contrast, global changes of surface salinity (32-38 pss) and temperature (0°C-30°C) only modify the Tb by ~5 K. So we believe such signal is very likely a natural extreme of sea surface emission at L-band over the oceans. Application of the GMF to retrieve surface wind-speed from the SMOS excess brightness temperature, we obtained the wind speed module shown in Figure 22, middle right panel. One can easily see that around the cyclone eye, wind speeds largely exceed the 64 knots threshold for typhoons within a more than 50 km radius. The spatial resolution of SMOS however does not allow to resolve the detailed wind speed structure around the eye. The maximum wind estimated from SMOS nevertheless reach an extremely high value of 142 knots.

Given the spatial resolution of SMOS, the wind speed estimated is more equivalent to a 10 minute sustained wind than to a 1 minute one, traditionally used by forecasters in the US. Using a 0.93 conversion factor from 1 mn to 10 mn winds (Harper et al., 2010), 1 minutes sustained winds can be estimated from SMOS. The evolution of the maximum sustained wind speed deduced from SMOS is compared to other estimates in Figure 22 bottom panels. SMOS estimate compares well with standard methods. The Advanced Dvorak Technique (ADT) utilizes longwave-infrared, temperature measurements from geostationary satellites to estimate tropical cyclone (TC) intensity. This step-by-step technique relies upon the user to determine a primary cloud pattern and measure various TC cloud top parameters in order to derive an initial intensity estimate. It continues to be the standard method for estimating TC intensity where aircraft reconnaissance is not available (all tropical regions outside the North Atlantic and Caribbean Sea), however it has several important limitations and flaws. The primary issue centers upon the inherent subjectivity of the storm center selection and scene type determination proceedures. Secondly, learning the Dvorak Technique and its regional nuances and adjustments can take a significant time to master. As evidenced in Figure 22 bottom left panel, ASCAT A & B maximum winds never exceeded hurricane force for this extremely intense Category 5 typhoon.

SMOS data provide a global coverage about every 3 days. During fast evolving storm events, SMOS swath can however miss interception with such fastly evolving storms or just capture a portion of the storm. In addition, SMOS data can be heavily contaminated in some areas by RFI, solar effects or land contamination. RFI are particularly problematic in the North west Pacific and in the Bay of Bengal. Combining SMOS and AMSR2 retrievals shall definitively help better characterizing high wind speed and storm events over the globe.

As shown in Figure 22, for the Hayian case, SMOS estimate compares very well with standard methods. Nevertheless, the SMOS sampling along the complete life cycle of the storm is limited to 4 usefull overpasses. Complementing the SMOS sampling with other sensors would be therefore certainly beneficial. With the recent developments of new methodologies to better retrieve surface wind speed in all weather conditions from X, C and L-band radiometer measurements from Space (Meissner and Wentz, 2009; El-Nimri et al., 2010, Reul et al., 2012, Zabolotskikh, 2015) the synergy of passive low-microwave frequency observations from space operating within the X to L-bands (AMSR2,WindSat, SMOS and SMAP) can now be envisaged. The complementarity and added-value with scatterometer ones (ASCAT & Oscat) and NWP products (ECMWF & NCEP) will be studied in more detailed in the frame of our on-going study with the aim to produce new blended surface wind speed products including the SMOS high wind speed data. As a first objective we started merging SMOS data and AMSR2 wind speed retrievals and will further add the WindSat data and the future SMAP sensor ones. For AMSR2 high wind speed retrieval under rain, we rely on the new methodology currently developed by Zabolotskikh et al., 2015. SMOS intercepted Haiyan on the 7 Nov 2013 at 09:15Z while AMSR2 intercepted the Typhoon the same day about 5 hours sooner at ~ 4:22 Z. Surface wind speed retrieved from both sensors for these two passes were compared in Zabolotskikh et al., 2015 showing excellent agreement between both estimates for the high wind region. Figure 23 is further illustrating the strength of the synergies and data merging between these two sensors in term of increased spatial and temporal coverage for rapidly evolving and intense storms such as Haiyan typhoon.

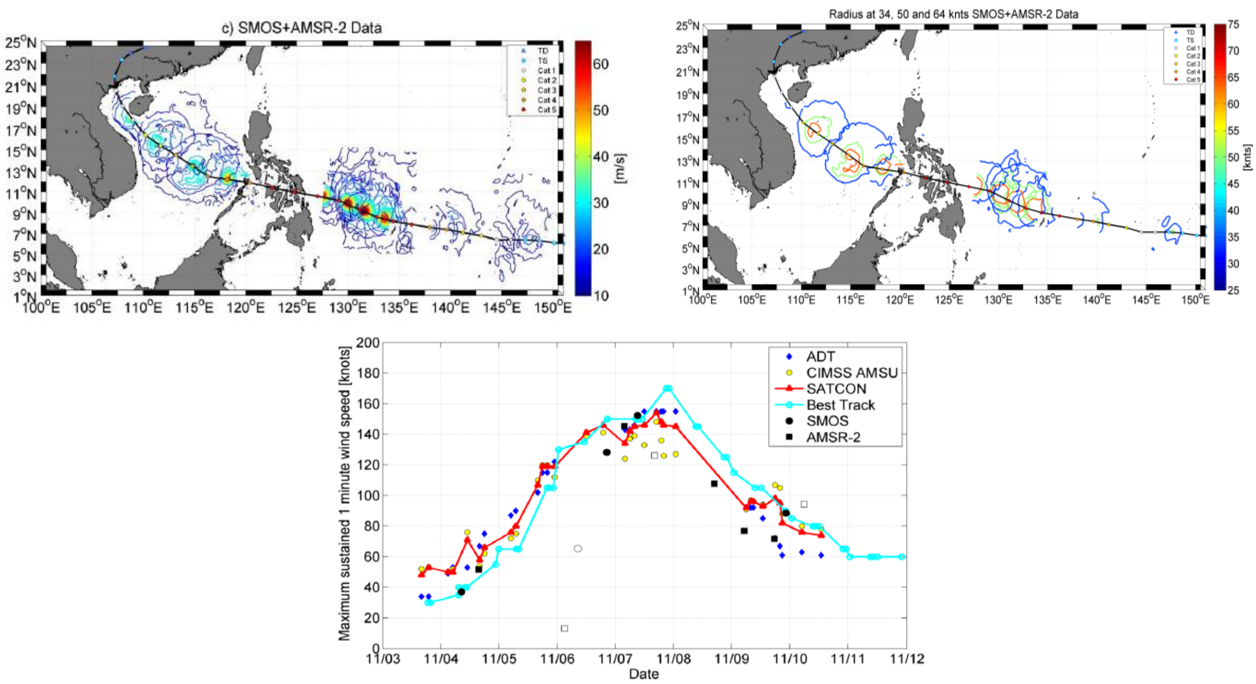

Figure 23: Top left: Surface Wind speed contours (from 0 to 70 m/s per 5 m/s steps) obtained by combining SMOS and AMSR-2 retrieved fields over Haiyan. Top right: wind radii at 34 (blue), 50 (green) and 64 (orange) knts obtained from the merged wind fields. Bottom: same than in bottom plots of Figure 23 but now showing SMOS (black circles) and AMSR-2 (black squares) retrieved maximum winds.

As shown in Figure 23, by combining both sensors, consistent and more continuous estimations of key parameters for describing the storm wind field structures in the context of improving NWP forecasts, such as radii at 34, 50 and 64 knots, and maximum sustained winds can now be provided and augmented.

Note finally that an on-going effort are also conducted to demonstrate the utility, performance and impact of SMOS- STORM products on TC and ETC prediction systems in the context of maritime applications. Comparisons of the SMOS wind speed data with short range forecasts of 10m winds from the Met Office global model background are now performed to generate observed minus background values (O-B). The impact of assimilating SMOS wind speeds will be soon demonstrated by diagnosing changes to the mean global atmospheric analyses e.g. low-level wind field, pressure at mean sea level (PMSL), etc.. Comparing various forecast variables (e.g. wind, surface pressure, geopotential height) with quality-controlled observations valid at the same time/location and calculating the difference in root mean square (RMS) error between the trial and control values will be conducted to show how changes in the analysis as a result of assimilating SMOS wind speed observations affect global model forecasts (so-called global NWP index).

7 ACKNOWLEDGEMENTS

We would like to acknowledge the support of ESA Support to Science Element program under the contract SMOS+STORM evolution, #4000105171/12/I-BG.

8 REFERENCES

Chavas, D. R, N. Lin, and K. A. Emanuel (2015), A model for the complete radial structure of the tropical cyclone wind field. Part I: Comparison with observed structure, Journal of the Atmospheric Sciences, doi: http://dx.doi.org/10.1175/JAS-D-15-0014.1

Donnelly, W. J., J. R. Carswell, R. E. McIntosh, P. S. Chang, J. Wilkerson, F. Marks, and P. G. Black(1999), Revised ocean backscatter models at C and Ku band under high-wind conditions, J. Geophys. Res., 104(C5), 11485–11497, doi:10.1029/1998JC900030.

Entekhabi, D., S. Yueh, P. O[1]Neill, K. Kellogg et al., SMAP Handbook, JPL Publication JPL 400-1567, Jet Propulsion Laboratory, Pasadena, California, 182 pages, 2014. - See more at: https://www.cuahsi.org/Posts/Entry/11508#sthash.K9plxnN0.dpuf

Houze, R. A., Jr., P. V. Hobbs, K. R. Biswas, and W. M. Davis, 1976: Mesoscale rainbands in extratropical cyclones. Mon. Wea. Rev., 104, 868-878.

Houze, R. A., Jr., F. D. Marks, Jr., and R. A. Black, 1992: Dual-aircraft investigation of the inner core of Hurricane Norbert. Part II: Mesoscale distribution of ice particles. J. Atmos. Sci., 49, 943-962.

Joyce, R. J., J. E. Janowiak, P. A. Arkin, and P. Xie, 2004: CMORPH: A method that produces global precipitation estimates from passive microwave and infrared data at high spatial and temporal resolution.. J. Hydromet., 5, 487-503.

Knapp, K. R., M. C. Kruk, D. H. Levinson, H. J. Diamond, and C. J. Neumann, 2010: The International Best Track Archive for Climate Stewardship (IBTrACS): Unifying tropical cyclone best track data. *Bulletin of the American Meteorological Society*, 91, 363-376**.** doi:10.1175/2009BAMS2755.1

Holthuijsen, L. H., M. D. Powell, and J. D. Pietrzak (2012), Wind and waves in extreme hurricanes, J. Geophys. Res., 117, C09003, doi:10.1029/2012JC007983.

Horstmann, J., C. Wackerman, S. Falchetti, and S. Maresca. 2013. Tropical cyclone winds retrieved from synthetic aperture radar. *Oceanography* 26(2):46–57, http://dx.doi.org/10.5670/oceanog.2013.30.

Mecklenburg S., Matthias Drusch, Yann H. Kerr, Senior Member, IEEE, Jordi Font, Manuel Martin-Neira, Steven Delwart, Guillermo Buenadicha, Nicolas Reul, Elena Daganzo-Eusebio, Roger Oliva, and RaffaeleCrapolicchio, “ESA’s Soil Moisture and Ocean Salinity Mission: Mission Performance and Operations”, IEEE TGARS, Vol 50, No 5, pages 0196-2892, 2012.

Powell, M.D., 2010: "Near-surface based, airborne, and satellite observations of tropical cyclones." *In Global Perspectives on Tropical Cyclones: From Science to Mitigation*, J.C.L. Chan and J.D. Kepert (eds.). World Scientific Publishing Company, 2nd edition, p. 177-199.

Quilfen Yves, Vandemark Doug, Chapron Bertrand, Feng Hui, Sienkiewicz Joe (2011). Estimating Gale to Hurricane Force Winds Using the Satellite Altimeter. Journal Of Atmospheric And Oceanic Technology, 28(4), 453-458. http://dx.doi.org/10.1175/JTECH-D-10-05000.1

Ruf, C., A. Lyons, M. Unwin, J. Dickinson, R. Rose, D. Rose and M. Vincent, "CYGNSS: Enabling the Future of Hurricane Prediction," IEEE Geosci. Remote Sens. Mag., **Vol. 1**, No. 2, 52-67, doi: 10.1109/MGRS.2013.2260911, 2013. [paper]

Reul Nicolas, Chapron Bertrand (2003). A model of sea-foam thickness distribution for passive microwave remote sensing applications. Journal of Geophysical Research Oceans, 108(C10), -. Publisher's official version : http://dx.doi.org/10.1029/2003JC001887.

Reul N., Tenerelli J., Chapron B., Vandemark D., Quilfen Y., and Y. Kerr, "SMOS satellite L-band radiometer: A new capability for ocean surface remote sensing in hurricanes", Journal of Geophysical Research, vol. 117, C02006, doi: 10.1029/2011JC007474, (2012).

Weissman, D.E., Bourassa, M. A. and Tongue, J. (2002) Effects of rain rate and wind magnitude on Sea Winds scatterometer wind speed errors. Journal of Atmospheric and. Oceanic Technology., 19, pp. 738-746

Young, I. R. 2003: "A Review of the Sea State Generated by Hurricanes ", Marine Structures. 16, 201-218

Zabolotskikh Elizaveta, Mitnik Leonid M., Reul Nicolas, Chapron Bertrand (2015). New Possibilities for Geophysical Parameter Retrievals Opened by GCOM-W1 AMSR2. IEEE Journal of Selected Topics in Applied Earth Observations and Remote Sensing, PP(99), 1-14. Publisher's official version : http://dx.doi.org/10.1109/JSTARS.2015.2416514.